Detection of abrupt changes in East Asian monsoon from Chinese loess and speleothem records

Denis-Didier Rousseau, Witold Bagniewski, Youbin Sun

Detection of abrupt changes in East Asian monsoon from Chinese loess and speleothem records

Denis-Didier Rousseau[1,2,3], Witold Bagniewski[4], Youbin Sun[5]

[1] Université Montpellier, Géosciences Montpellier, Montpellier, France

[2] Silesian University of Technology, Institute of Physics-CSE, Division of Geochronology and Environmental Isotopes, Gliwice, Poland

[3] Columbia University, Lamont Doherty Earth Observatory, New York, USA

[4] Ecole Normale Supérieure – Paris Sciences et Lettres, Laboratoire de Météorologie Dynamique, Paris, France

[5] Chinese Academy of Sciences, State Key Laboratory of Loess and Quaternary Geology, Institute of Earth Environment, Xi'an, China

HIGHLIGHT:

- Abrupt transitions in loess grain-size and speleothem $\delta^{18}O$ records can be automatically detected.
- Our detection approach can facilitate the correlation of abrupt monsoon changes over the last 3.6 Myr.
- The winter monsoon strength increased over 3 main steps during the past 3 Myr.
- Major tipping points can be employed for synchronizing paleoclimate records on a global scale.

ABSTRACT:

Abrupt climate changes, especially at millennial timescales, have become a key topic in paleoclimatology because of their link with the tipping point theory and their extensive impacts on future climate scenarios. Although best documented in ice-cores and marine sediments, they are also recorded in different archives on the land, among which Chinese loess and speleothem records are of particular interest. These records effectively document orbital-to-millennial monsoon variability during the Pleistocene, but the dominant periodicity revealed by proxy records from these two types of archives is different. Nevertheless, millennial-scale oscillations recorded in Chinese loess and speleothem records seem highly similar over the last several glacial cycles. Such millennial fluctuations can be of varying amplitudes, and either more or less abrupt depending on the type of record. The observed abruptness usually depends on the sedimentation rates and sampling resolution in the loess and speleothem records. However, it can also be refined by comparisons with multiple physicochemical and isotopic proxies. Here, we apply a robust statistical method to detect abrupt changes in loess grain size and speleothem $\delta^{18}O$ records. As a first step, we compared two reference records (i.e. the NGRIP ice-core and the Hulu speleothem $\delta^{18}O$ records) of abrupt climate change to verify the robustness of our method in detecting the well-recognized abrupt events during the last glaciation. This result allows us, in a second step, to compare two high-resolution loess grain-size stacks (i.e. the CHILOMOS, and the LGS640 datasets) with the Chinese speleothem composite record built from Hulu and Sanbao records. Although visually observed rapid grain-size variations were previously interpreted as representing millennial-scale variations, our statistical analysis confirms that whether these abrupt climate changes can be robustly identified is highly dependent on the time resolution of the studied records. In a third step, we

detected abrupt transitions in the MGSQ grain size stack, covering the last 3.6 Myrs. Our results also show that both winter and summer monsoons co-varied at glacial-interglacial to millennial timescales, reflecting a three-stage evolution of increasing intensity: (1) from 3.6 Ma to 2.6 Ma, (2) from 2.6 Ma to 1.2 Ma, and (3) from 1.2 Ma to present. Our results finally show that the identified abrupt climate events can be employed for synchronizing climate records on a global scale.

Keywords: Abrupt climate transitions, Chinese loess sequences, Millennial scale variability, Grain size, East Asian Monsoon, stepwise increasing of the monsoon intensity.

1. Introduction

Chinese loess records are among the most valuable continental archives of past climate changes, particularly due to the exceptional dust trap that northern China has constituted through time, allowing a quasi-tabular deposition of the eolian sediment forming the Chinese Loess Plateau (CLP) (Liu and and collaborators, 1985; An, 2000). Contrary to European and North American sequences, the Chinese loess sequences display a quasi ”simple” alternation between loess units, corresponding to even glacial stages and paleosol complexes corresponding to odd marine isotopic stages (Liu and Ding, 1998; Ding et al., 2002; Sun et al., 2006). Such alternating loess-paleosol sequences can be easily traced across the CLP, facilitating the correlation between loess records over North-South or West-East transects, but also with the marine isotope stratigraphy. The Quaternary loess deposits overlay the Red-Clay formation which spatial distribution differs from that of the Quaternary loess-paleosol sequences (An et al., 2014). The basal age is about 8-7 Ma, (Ding et al., 1999; An, 2000) in middle CLP and 11 Ma in eastern CLP (Xu et al., 2009). Red Clay formation is also of eolian origin (Lu et al., 2001; Li et al., 2006, 2008), and displays alternations of units similar to those observed in the Quaternary sequence (Ding et al., 1995; Liu and Ding, 1998). Furthermore, older Red Clay formation has been described, starting between 25 and 22 Ma based on the robust magnetostratigraphic dating of key sequences from the western CLP (Guo et al., 2002; Qiang et al., 2011). By combining this precise magnetostratigraphy with other dating techniques, a complete chronostratigraphic frame has been built for the Chinese loess sequence, making it a key continental paleoclimatic archive.

As Chinese loess deposits are composed mainly of eolian dust transported from the Northern Chinese deserts (Sun et al., 2020), dust grain size is a well acknowledged paleoclimate proxy used to reconstruct past monsoon variations, especially atmospheric circulation over the last 8 Myrs (Ding et al., 2000; Sun et al., 2008, 2010). Indeed, numerous studies have shown that the grain size from the loess units is coarser than that of the paleosol complexes, which has been interpreted as reflecting stronger East Asian winter monsoon (EWWM) strength from the desert sources to the CLP, (e.g. An et al., 1991; Xiao et al., 1995). Numerous luminescence dates obtained from the loess sequences allows refining their chronology of loess deposits since the last interglaciation (Lu et al., 2007; Lai et al., 2007; Sun et al., 2012). The grain-size variations of sequences with a high sedimentation rate can well record millennial scale variability based on comparison with Chinese speleothem and Greenland ice core records (Sun et al., 2012; Yang and Ding, 2014; Sun et al., 2021). However, millennial-scale variability recorded in the loess deposits is usually identified by visually comparing the grain size variations and either the $\delta^{18}O$ fluctuations from the NGRIP (Rasmussen et al., 2014) and the Chinese composite speleothem (CS) records (Cheng et al., 2016), which both hold a more global significance.

In our study, we are testing the occurrence of abrupt transitions in three high resolution grain-size stack records from Chinese loess sequences covering respectively the last 250 kyrs (Yang and Ding, 2014), the last 640 kyrs (Sun et al., 2021), and the last 3.6 Myrs (Sun et al., 2006). In the first section, we compare the abrupt transitions detected from the NGRIP and CS using the Kolmogorov-Smirnov (KS) test. We demonstrate therefore the reliability of our method, and then use the composite CS record as a reference record for the following grain-size record analyses. In the second section, we compare the abrupt transitions detected in the different grain-size stacks of varying length and time resolution and in CS by applying Recurrence Quantification Analysis (RQA), which is mainly useful in characterizing the key transitions (Bagniewski et al., 2021, 2023; Rousseau et al., 2022). In the third section, we detect the main abrupt transitions from the grain size record of the last 3.6 Myrs. Analytical results and paleoclimatic implications are described in the final section.

2. Material and Methods

2.1. Material

The CHILOMOS (CHInese Loess Millennial-scale Oscillation Stack) grain-size stack record, covering the last 250 kyrs, is built from eight sequences located in the northern CLP where high-sedimentation-rate loess sequences can provide the greatest likelihood of capturing abrupt transitions over the last two glacial cycles (Yang and Ding, 2014). CHILOMOS dataset includes up to 65 m of alternating loess-paleosol sequences, totaling 12,330 samples. The grain-size record is expressed by the median size in phi scale, where lower values indicate coarser grain-size. The time resolution is 200 years. The LGS640 (Loess Grain-Size stack spanning the last 640 ka) shows the average grain size from three high-resolution sequences from the western CLP, namely Gulang, Jingyuan, and Linxia. The thickness of the record varies between 151.4 to 164.2m, where higher values indicate coarser grain sizes. The LGS640 time scale has been refined by comparison with the speleothem chronology (Cheng et al., 2016), with a time resolution of 100 years (Sun et al., 2021). Finally, the MGSQ (Mean Grain-Size of Quartz particles) 3.6 Myrs stack record, built from two loess-paleosol-red clay sequences in the central CLP; both consists of the complete Quaternary loess-paleosol alternations (166 m and 168 m respectively) and the upper Red Clays formation of Pliocene age (120 m and 55 m respectively). The MGSQ record is built from quartz particles extracted from samples taken at 8 cm and 10 cm intervals in the Quaternary deposits, and at 4 cm and 5 cm intervals in the Red Clay. The grain size has been normalized, with lower values corresponding to the coarser grain size particles. The MGSQ timescale has been established by magnetostratigraphy and orbital tuning to obliquity and precession and the time resolution is 1000 years (Sun et al., 2006).

The Chinese speleothem (CS) $\delta^{18}O$ composite record is built from different Chinese speleothems covering the last 640 kyrs with a 22-year resolution (Cheng et al., 2016). This record characterizes the variations in the East Asian Monsoon as a direct response to the summer insolation at 65°N on orbital scale, with lower $\delta^{18}O$ values corresponding to a higher East Asian Summer Monsoon (EASM) intensity. Millennial-scale variations are superimposed with the orbital scale variations, with their intensity and duration decreasing during the glacial time intervals in comparison to the interglacial ones. The interstadials nomenclature used, for the last 250 kyrs in the present study, corresponds to that applied to both Hulu and Sanbao cave records by Wang et al. (2008) and Cheng et al. (2016).

The NGRIP $\delta^{18}O$ record is the reference time series for Northern Hemisphere climate variations over the last 122 kyrs with a time resolution of 20 years (Rasmussen et al., 2014). It is characterized by abrupt warmings of about 12°C on

average over Greenland (Kindler et al., 2014), which occur over a period of approximately 50-100 years, (Wolff et al., 2010; Rousseau et al., 2017a) corresponding to the canonical Dansgaard-Oeschger events (DOs) (Dansgaard et al., 1993) or Greenland Interstadials (GI). Their duration, on an average of about 1,050 years, varies during the last climatic cycle with the shortest DOs or GIs occurring during the time equivalent to Marine Isotope Stage 3, e.g., between 57 ka and 29 ka b2k. Every interstadial is followed by a more gradual two-stepped return to glacial conditions, i.e. a Greenland stadial (GS). Moreover, Rasmussen et al. (2014) identified some abrupt cooling events within the canonical DOs that they labeled using a "b", "d", or "f" associated with the GI number, for example GI-22f.

In the original study of the Hulu Cave record, $\delta^{18}O$ values ranged from -4 to -9‰ between 75 and 10 ka (Wang et al., 2001, 2008). These variations have been interpreted as corresponding to changes in the summer/winter precipitation ratio over time. Moreover, the Hulu record shows numerous millennial-scale events characterized by shifts in $\delta^{18}O$ over short time intervals. These abrupt variations mimic the Greenland ice-core $\delta^{18}O$ records, which are interpreted in terms of temperature variations, on a similar timescale. Accordingly, moistening events (minimum $\delta^{18}O$ values) in the Chinese speleothem correlate with warming (interstadial) events in Greenland. By contrast, drying events (maximum $\delta^{18}O$ values) in the Chinese speleothem record correlate with cooling (stadial) events in Greenland. Such interpretation of the Chinese speleothem $\delta^{18}O$ values has been applied to the whole composite speleothem record.

2.2. Methods

The first method applied to detect abrupt transitions in our datasets is the augmented KS test as defined in Bagniewski et al. (2021). A two-sample KS test is employed to compare values on either side of a value of proxy *X* at time *t* (X_t) which could indicate a significant change in the paleoclimate record. Given a high enough time resolution of the paleorecord, the frequency with which the KS test detects transitions will largely depend on its window length. The window length is considered inadequate if it is significantly shorter or longer than the time interval between two discontinuities (Bagniewski et al., 2021). Therefore, to optimize the analysis for the most relevant time scale, Bagniewski et al. (2021) introduced a varying window length between 0.6 and 4 kyr, which corresponds to the time scale at which the given paleorecords were investigated. The KS statistic is calculated for all window lengths to identify abrupt transitions, with values above 0.7 considered significant. We first identify transitions using the longest window, which has the largest sample size and therefore the greatest statistical significance. Subsequently, transitions detected using shorter windows are incorporated to capture transitions on shorter time scales. Finally, to identify transitions between dominant climate modes, such as Stadial-Interstadial (GS-GI) boundaries in the NGRIP record, we employ a running window to determine the upper and lower values of the time series and find transitions that signal a switch from one mode to the other. More detail is given in Bagniewski et al. (2021). The three datasets presented previously have been analyzed using the same window lengths.

To gain further insights into the abruptness or transitions of past climate changes, we performed a quantitative analysis of these time series of proxy variables using recurrence plots (RPs). RPs were introduced to the study of dynamical systems by Eckmann et al. (1987), while a quantification of RPs was developed by Zbilut and Webber Jr. (1992), and further popularized in climate studies by Marwan et al. (2007, 2013). The purpose of RPs is to identify recurring patterns in time series, such as in paleoclimate records. The RP for a time series $\{x_k : k = 1,\ldots,N\}$ is constructed as a square matrix in which both axes represent time. A dot is entered into a position (i, j) of the matrix when $|x_i - x_j| < \varepsilon$,

with ε being the recurrence threshold. Eckmann et al. (1987) distinguished between large-scale *typology* and small-scale *texture* in the interpretation of a square matrix of dots that is the visual result of RP. The most interesting typology in RP applications is associated with recurrent patterns that are not exactly periodic and thus not easily detected by traditional spectral analysis methods. Marwan et al. (2007) discuss how to make the purely visual RP typologies more objectively quantifiable through the use of recurrence quantification analysis (RQA). In our analysis, we quantified the Recurrence Rate (RR) of the time series, which describes the probability of states of the system recurring within a particular time interval. For the datasets presented in this study, the RR is calculated using a 4kyr-sliding window, and plotted together with the recurrence plot. Following the RR prominence analysis (Bagniewski et al., 2021), the minima of the RR are identified, corresponding to abrupt transitions of interest. These major rapid changes are marked on the figures with pink crosses and discussed later in the paper.

3. Results

3.1. Comparison between NGRIP and the Chinese speleothem records: the last climate cycle (Fig. 1 and Table 1)

These two records have been obtained through different proxies and dating methods, as previously noted, but have a similar time resolution of 20-22 years. Both records show similarities in terms of detected abrupt transitions, including abrupt warmings (DOs or GIs) in Greenland or intensified EASM (A events), as well as coolings corresponding to transitions to stadials (GS) in the polar region or drier conditions of intensified EAWM over CLP. The latter events have been labeled SAx in our study for stadials following A events. The comparison between the two records shows 17 similar warming transitions versus 12 similar cooling ones (**Table** 1).

When dividing both records into three main time intervals, 122 ka - 84 ka, 84 ka - 46 ka and 46 ka – 8 ka, one can notice an increasing number of similar abrupt transitions, with 6 in the oldest interval, 10 in the middle interval, and 14 in the youngest interval. Interestingly, although the main DOs or GIs are identified, some of them are not detected by the KS method. This is the case for GI-9, GI-6, GI-4, GI-3, and GI-2 in the NGRIP record, as well as A9 and A3 (equivalent of GI-9 and GI-3 in the CS) for the most recent interval. In the middle interval, the KS method does not detect the abrupt transitions toward GI-19.1, GI-18, and GI-15 in NGRIP, as well as A15, the equivalent of GI-15 in CS. Finally, the abrupt change towards GI-23.2 in the NGRIP record and A25, the equivalent of GI-25 in the CS record, are not detected by the KS method (**Fig.** 1).

The KS method successfully detects numerous known transitions from interstadials to stadials in the previous three different time intervals. However, it still misses some of them like the transition toward GS-9, GS-4, GS-3 and GS-2 in the NGRIP record and toward SA10 and SA2, the equivalent of GS-10 and GS-2 in the CS series. In the second interval, more transitions are not detected, especially in the CS record: toward GS-18, GS-17, and GS-15 in NGRIP record and towards SA19.1, SA18, SA17, SA16, and SA14, the equivalents of GS-19.1, GS-18, GS-17, GS-16, and GS-14 in CS. Finally, the KS method does not detect the abrupt transition towards GS-23.1 in NGRIP and toward SA15, the equivalent of GS-25 in CS, in the third time interval (**Fig.** 1,2).

The very good agreement in the millennial scale variability of the two different climate proxies supports the original interpretation of a close relationship between abrupt warmings in Greenland and intensified summer monsoon events in China (see **Fig.** 1). Such a result gives us confidence for using the Chinese speleothem composite record as a reference for

the detection of the potential millennial variability in the CHILOMOS and LGS640 grain-size stacks over the last several glacial-interglacial cycles.

3.2. Comparison between the composite Chinese speleothem and the CHILOMOS grain size stack: the last two climate cycles

3.2.1. KS test (Fig. 2 and Table2)

Following the analysis in the previous section, the abrupt changes detected from CS have been interpreted as corresponding to either the warming or the cooling transitions observed in the polar region. The Chinese interstadials, representing intervals of warming or intensified summer monsoon, are labelled Ax for the last climate cycle and Bx for the penultimate cycle, following Cheng et al. (2006) and Wang et al. (2008). Similarly, stadials of the last climate cycle are labelled SAx, while the stadial equivalents of the penultimate cycle are denoted with the label SBx.

The KS test mostly detects the warming/moistening transitions already published, although it is missing some of the them, 5 in the last climate cycle (A25, A15, A13, A9 and A3), and many more, 9, in the penultimate cycle (B22, B18, B14, B9, B6, B5, B4, B2, B1) (Fig. 2 and Table 2). Fewer robust abrupt transitions are detected in CHILOMOS than in CS. Due to the lower resolution of this record, the warming transitions appear more gradual than abrupt, in contrast to the speleothem $\delta^{18}O$ record. Compared to the published changes related to abrupt climate variability, 13 have not been detected by the KS test for the last climate cycle. This is consistent with the findings for the penultimate cycle, where 13 published transitions have not been detected among the original 26 (**Table** 2). Regarding the transitions towards stadial/drying intervals, the KS test has detected 21 in the penultimate climate cycle and 26 for the last climate cycle in CS, compared to 12 and 14 respectively in CHILOMOS.

The difference in the time resolution of the two records also limits the number of common abrupt transitions detected, with a total of 23, 9 in the penultimate climate cycle and 14 in the last one (Fig. 2). The number of drying changes, 14, exceeds that of moistenings, 9 (**Fig.** 2). Therefore, both CHILOMOS and CS records share abrupt moistening transitions towards the relatively short interstadial-like events, B17, B12, B11, A19, A16, A14, A12, A8 and A2 from the oldest to the youngest (see **Fig**. 2). Similarly, both records share abrupt transitions towards drier, longer stadial-like events SB20, SB19, SB14, SB13, SB2, SA24, SA21, SA20, SA13, SA12, SA8, and SA4 also from the oldest to the youngest. When comparing the KS test on the NGRIP and CS $\delta^{18}O$ and CHILOMOS grain size records, six common moistening and three common drying events are detected at about the same date with differences, between the oldest and the youngest dates identified, varying between 85 and 1,160 years (see **Suppl. Table 1**)

3.2.2. RQA (Fig. 3, 4 and Table 3)

The recurrence plots of CS and CHILOMOS display two distinct patterns. Although the RP of the speleothem record exhibits a drift topology characteristic of a monotonic trend in variability, which corresponds to a clear monsoon signature of 20 kyr (**Fig.** 3), this is not the case for CHILOMOS. The RP of the composite grain-size shows various clusters, which roughly correspond to specific periodic patterns. More precisely, these clusters reproduce the main marine isotope stages described for the last two climate cycles (**Fig.** 4).

The analysis of the recurrence rates identifies 25 significant minima in both records with a recurrence rate prominence higher than 0.5, 12 in CHILOMOS and 13 in the speleothem records (**Table** 3). Furthermore, 9 minima of the

RR appear common to both the CS and the grain-size records, most of which occurred during the last climatic cycle and were identified by the KS method (see **Table** 3 with values highlighted in yellow).

3.3. Comparison between the composite Chinese speleothem and the LGS640 grain size stack: the last seven climate cycles (Fig. 5, 6 and Table 4,5).

3.3.1 KS test (Fig. 5 and Table 4)

98 abrupt transitions have been detected from the LGS640 grain size stack, which can be broken down into 49 abrupt increases and 49 abrupt decreases in size properties, indicating key climate changes. Several of them correspond to the transitions between marine isotope stages (see **Fig.** 5). Moreover, contrary to what could be expected from a visual inspection of the record, not all abrupt variations observed during glacial conditions are detected as significant abrupt transitions when using a window size of 0.6-4 kyrs in the KS test. Nevertheless, the abrupt transitions towards higher grain size are still better identified during glacial intervals, even marine isotope stages, across all climate cycles seen in the record except for the 2 oldest ones.

The comparison of the 103 detected abrupt transitions in LGS640 with the 171 transitions identified in the CS record of the last seven climate cycles shows an unbalanced ratio (Table 4). The number of transitions detected from the $\delta^{18}O$ are rather even (86 dryings versus 85 moistenings over 640 kyrs) although those detected from the average grain size show a higher number of dryings (55) than of moistenings (46) over 660kyrs. In both records, the last 2 climate cycles show the highest number of abrupt transitions detected compared to the oldest cycles (see **Suppl. Table** 2,3). Over the past 640 kyrs covered by both LGS640 and composite speleothem $\delta^{18}0$, the KS test has detected equally 24 abrupt transitions towards drying and moistening events. However the maximum difference dates (CS minus LGS640) detected is the highest for the drying transitions (2,950 years) versus 800 years for the moistening ones. On the contrary, the minimum difference is about the same for both types of transitions, 750 years for moistening and 900 years for drying events (see **Table** 4).

3.3.2. RQA (Fig. 6 and Table 5)

The recurrence plot of LGS640 shows two main clusters corresponding to the last 627 kyrs and the oldest part of the record. This is mainly due to the very high values of the average grain size at 630 kyrs. The younger cluster can be further divided into two, with a transition observed at 336 kyrs. These two dates correspond to the highest RR prominence values, found at the start of two climate cycles, MIS 16-15 and MIS 10-9 respectively. They also are characterized by the higher values in the average grain size. Among the following detected transitions with a high RR prominence are the different boundaries between the successive climate cycles at 427 ka and 130 ka for MIS12/11 and MIS 6/5 respectively, and including the start of MIS 12 at 476 ka. Other significant abrupt transitions are detected as well, but exhibiting much lower RR prominence (see **Fig.** 6 and **Table** 5).

3.4. Abrupt transitions over the last 3.6 Myrs from the MGSQ *stack (Fig. 7, 8 and Table 6).*

3.4.1 KS test (Fig. 7 and Table 6)

Contrary to the previous analyses, the abrupt climate changes detected in the MGSQ sequence are mainly corresponding to cooling and warming transitions observed in the marine isotope stratigraphy (Lisiecki & Raymo, 2005).

The KS method is relatively inefficient in detecting boundaries between the marine isotope stages for the last interval (3.6 – 2.6 Ma), but detects many more boundaries for the 2.6 – 1.2 Ma interval, and almost all those described for the last 1.2 Myrs (**Table** 6). The difference between these three time intervals illustrates varied magnitude of the grain-size variations over the past 3.6 Myrs in the CLP (see **Fig.** 7).

3.4.2. RQA (Fig. 8 and Table 6)

The recurrence plot of MGSQ shows two main clusters, one corresponding to the 3.6 Ma to 2.7 Ma time interval and the other corresponding to the last 2.6 Myrs, with a small transition between 2.7 Ma and 2.6 Ma. The oldest cluster, roughly of Pliocene age, can be decomposed into two around a 3.14 Ma threshold, which corresponds to a strong increase in grain-size. This transition marks a shift from the low values observed during the Pliocene to the higher values characteristic of Quaternary deposits. The younger cluster of Quaternary age displays a nearly monotonic trend, although the previously analyzed stacks indicate that some variability can be detected. The analysis of the recurrence rates identifies numerous significant minima, among which the first eight have a recurrence rate prominence higher than 0.6 (**Fig.** 8 and **Table** 6). Among them, 1.25 Ma and 2.6 Ma are the most dominant transitions and correspond to main boundaries detected by the KS method (see **Table** 6).

4. Discussion

The Chinese speleothem loess records show abrupt variations of East Asian monsoon during the studied climate cycles. Almost all the abrupt changes previously described, synchronous with the Greenland interstadials and identified by labels A, are detected by the KS and RQA methods. Some events, however, remain undetected, mainly those labeled with Bs in the penultimate climate cycle, though they are few in number. The close correspondence in the detected abrupt transitions between the Chinese speleothem and the Greenland NGRIP ice-core for the last climate cycle clearly indicates that both the Polar region and East Asia have been impacted by the millennial-scale variability of the climate occurring in the Northern Hemisphere. The identification of similar patterns in the older climate cycles of CS clearly demonstrates that this millennial-scale variability prevailed also during the previous climate cycles, i.e., the 640 ka - 130 ka interval, although no corresponding record is presently available from Greenland. The RP of the climate cycles of CS also shows that this millennial-scale climate variability was modulated by a predominantly 20 kyr signal over the past 250 kyrs (**see Fig.** 3), indicating a dominance of precession forcing, and thus demonstrating a summer monsoon signature that has been previously discussed for the whole record (Cheng et al., 2016).

By comparison, the CHILOMOS record shows grain-size variations during glacial intervals that cannot be interpreted as clear abrupt transitions by either the KS or RQA methods. This is related to the lower time resolution available, which is 10 times lower than that of the speleothem. This corresponds to the process followed to compile the eight sequences by Yang and Ding (2014). Nevertheless, the comparison of the KS results from both CS and CHILOMOS series indicates that they both recorded the millennial-scale variability (**Fig.** 2). Although the RP of the speleothem displays the summer monsoon signature, that of CHILOMOS indicates 2 clusters corresponding to the last two climatic cycles, within which sub-clusters clearly characterize the different marine isotope stages, from MIS7-MIS6 to MIS5-MIS2 respectively, with MIS1 (the Holocene or the last 14.7 kyrs) represented separately.

One key point to notice is that the two types of records have two different sources, Northern Chinese deserts for the loess sequences, and the neighboring oceans/seas for the speleothem. The observed millennial-scale variability in both

types of records is interpreted as corresponding to the fingerprints of the abrupt climate variations occurring in the northern polar area and propagated southeastwards through the EAWM mechanism, with the CHILOMOS and CS characterizing the winter and summer monsoon regimes respectively. The DO/GI variability has been previously interpreted as resulting from the rapid retreat and slow regrowth of thick ice-shelves associated with variations in the Northern Hemisphere ice sheet volume. Accordingly, changes in sea-ice thickness are driven by changing subsurface water temperatures in the Northern Atlantic due to insulation by ice cover and variations in the AMOC strength (Boers et al., 2018). During GS, the ice-cover increased, preventing the warm subsurface water from reaching the North Atlantic area, resulting in a general cooling of the Northern Hemisphere temperatures and an increase in the atmospheric heat transport. This increased meridional temperature gradient over the Northern Hemisphere induced a stronger westerly circulation, resulting in stronger winds over Eurasia (Sima et al., 2009, 2013), reinforcing the Siberian High and thus the atmospheric circulation over the dust sources of the Chinese Loess Plateau (Sun et al., 2012).

At the same time, this particular regime weakened the cyclonic circulation over the sub-tropical western Pacific region and therefore reduced the SE inland moisture transport to the loess plateau (Sun et al., 2012; Yang and Ding, 2014). Loess units have been deposited during GSs over Europe (Rousseau et al., 2017b), as well as in the Loess plateau, but are characterized by coarser material, while higher $\delta^{18}O$ in the CS indicate moisture reduction (SB and SA events). During GIs, the warm subsurface waters transported by a strengthened AMOC, could have reached the North Atlantic region, leading to a general warming of the Northern Hemisphere and a demise of the ice cover and a possible collapse of ice-shelves. The resulting meridional heat gradient was much lower than in stadial conditions, inducing a weaker westerly circulation and weaker winds over Eurasia (Sima et al., 2009, 2013), causing higher temperatures that led to the development of paleosols (Rousseau et al., 2017a), and a much weaker Siberian high. The atmospheric circulation over the dust sources was weaker in the Chinese northern deserts, corresponding to the transport of much finer eolian material towards the loess plateau. The weakening of the Siberian high resulted in a stronger tropical cyclonic circulation over West Pacific, thus increasing the inland moisture transport that favors the development of the speleothem sedimentation. This is represented by the B and A events, marked by the lowest $\delta^{18}O$ values.

The longer LGS640, although having a 100-year time resolution, shows transitions that have been already detected in the CHILOMOS record for the last 250 kyrs, but also for the previous climate cycles. Table 4 indicates that some of the abrupt changes in the grain size correspond to boundaries between climate cycles as well as between some marine isotope stages. However, some of the transitions detected by both the KS test and RQA also correspond to abrupt transitions identified in the CS composite record (Fig. 5, 6 and Tables 4,5), implying that the interpretation proposed above remains valid for the entire 640 kyr interval.

Such detailed interpretation can be applied to the longer MGSQ record despite its time resolution of 1 kyr being much lower than the 100 or 200 yrs of LGS640 and CHILOMOS respectively, and especially the 22 yrs of CS. The abrupt transitions detected in MGSQ using the KS test correspond to the main transitions described in the marine isotope record, i.e., terminations and boundaries between glacials and interglacials. This shows that the grain-size variations on glacial-interglacial timescale follow those of the marine $\delta^{18}O$, which mainly reflect the variations of the northern hemisphere ice sheets. However, considering that the quartz particles were transported by winter monsoon winds, the coarser particles indicate stronger wind velocity for the EAWM conditions and, consequently, the Siberian High. The main abrupt transitions detected show that the winds associated with the EAWM at the base of the record, 3.6 Ma – 2.74 Ma, were significantly weaker than indicated by the grain-size values observed for the last climate cycle. Only the single event

at 3.144 Ma corresponding to the transition to MIS KM12 shows stronger winds during this first interval. The transition between 2.74 Ma and 2.6 Ma reveals an increasing trend in grain-size towards coarser grains from 2.6 Ma. This increasing trend in wind intensity corresponds to the growth of the northern hemisphere ice sheets, from mountain glaciers during the 3.6 Ma-2.74 Ma interval to fully developed ice caps (Naafs et al., 2013; Rousseau et al., 2022). Such evolution of the northern ice sheets marks an important shift in the climate system from earlier warm conditions, with the northern hemisphere ice sheets becoming a dominant factor in the climate system as they continued to grow over the last 2.6 Myrs (Ding et al., 2000; Rousseau et al., 2022). The second main threshold at 1.25 Ma corresponds to a new major event in the grain-size record with once more very coarse material transported by particularly strong winds. The interval 2.6 Ma – 1.25 Ma saw stronger winds during most odd marine stages than in the previous time interval, but weaker than during the later climate cycles. This interval, also called Lower Pleistocene, saw climate changes dominated by obliquity-paced variations.

The 1.25 Ma commonly marks the start of the Mid-Pleistocene Transition (MPT) interval during which the climate system shows a shift from cycles of about 40 kyrs to 100 kyrs (Pisias and Moore, 1981; Ruddiman et al., 1989; Clark and Pollard, 1998; Clark et al., 2006; Elderfield et al., 2012), characterized by the increasing magnitude of the fluctuations between glacials and interglacials. This interval lasts up to 0.87 Ma, which also corresponds to the main abrupt transitions detected by the RQA. During the MPT, northern hemisphere ice sheets expanded, and the first regular ice rafted debris (IRDs) deposits associated with odd marine isotope stages were observed at 1.5 Ma in Northern Atlantic cores (Hodell and Channell, 2016). The impact of this evolution of the northern hemisphere ice sheets on the quartz particle transport during MPT is not fully evident,, as some odd MIS are not well recorded in the MGSQ record. This could indicate that the potential relationship between the EAWM intensity and the development and expansion of the northern hemisphere ice sheets was not yet fully established. Interestingly, the 0.87 Ma date detected by the KS and RQA methods coincides with the proposed start of the millennial variability expressed by the DO/GI events (Rousseau et al., 2022). Moreover, the RQA detects 0.66 Ma as a key abrupt transition with high values in the grain–size records that the KS method identifies as well. This abrupt transition is also detected in the LGS640 record by the RQA method and corresponds to the first occurrence of massive iceberg calving, stronger that the ones leading to the regular deposition of IRDs in the North Atlantic cores, known as the Heinrich events (HE) (Hodell and Channell, 2016; Rousseau et al., 2022). These events signify a new step in the development and expansion of the northern hemisphere ice sheets reaching their biggest volumes of the past 2.6 Myrs. The last two dates at 0.426 Ma and 0.336 Ma represent the most recent time interval during which the highest amplitude between interglacials and glacials is observed in the global $\delta^{18}O$ record. During this time, the highest variations in transport of coarser and finer quartz grains in MGSQ were observed. Therefore, the EAWM intensity reached its maximum during this final interval in Earth's history. This evolution of MGSQ variations in three main steps supports the original interpretation of Sun et al. (2006) but with slightly different dates for the two oldest intervals, and introduces the Plio-Pleistocene transition (2.7 Ma - 2.6 Ma), the Mid-Pleistocene transition, and the Mid-Brunhes shift towards the maximum amplitude between glacials and interglacials of the last four climate cycles.

5. Conclusion

Abrupt climate transitions in Chinese loess sequences have been described in the literature for different time intervals. However, comparison of loess grain-size records with other proxies such as the composited Chinese speleothem $\delta^{18}O$ record remain providing questionable understanding of orbital- and millennial-scale variations of the East-Asian monsoon. Our analysis reveals that a robust detection of abrupt transitions is possible for these proxy records. Two high-resolution records (i.e. the Greenland NGRIP ice core $\delta^{18}O$ and the Hulu cave $\delta^{18}O$) were firstly compared to verify that our method can successfully detect the millennial variability for the last climate cycle. Similar findings are also evident for the penultimate cycle when comparing the composited Chinese speleothem $\delta^{18}O$ record (CS) (Cheng et al., 2016) and the CHILOMOS loess grain-size stack. The agreement between the transitions recorded in and and loess grain-size stack (i.e. CHILOMOS (Yang and Ding, 2014) and LGS640 (Sun et al., 2021)) allows to evaluate the co-evolution of millennial variability between winter and summer monsoons. Moreover, the analysis of the composite mean grain-size of quartz particles (MGSQ) (Sun et al., 2006) reveals that the main abrupt transitions detected correspond to the boundaries of the marine isotope stratigraphy. Most of these transitions therefore correspond to the so-called terminations from glacials to interglacials or inceptions from interglacials to glacials. Our analysis also supports the initial interpretation of stepwise strengthening of the winter monsoon associated with the onset and full development of the Northern Hemisphere ice sheets. Our results highlight the potential of abrupt changes as tie points for synchronizing different proxy indicators on a global scale, as recently demonstrated by Bagniewski et al. (2023)

Declaration of Competing of interest

The authors declare that they have no known competing financial interests or personal relationships that could have appeared to influence the work reported in this paper.

Data availability

The tables generated by this paper will be submitted to a PANGAEA data repository. NGRIP data are available at https://www.iceandclimate.nbi.ku.dk/data/GICC05modelext_GRIP_and_GISP2_and_resampled_data_series_Seierstad_et_al._2014_version_10Dec2014-2.xlsx (Rasmussen et al., 2014). The CHILOMOS grain-size data are available as supporting material at https://doi.org/10.1002/2013GC005113. The LGS640 stack data are available in the East Asian Paleoenvironmental Science Database (http://paleodata.ieecas.cn/index_EN.aspx. Finally the MGSQ data are available at https://www.ncei.noaa.gov/access/paleo-search/study/5602

Acknowledgement

Denis-Didier Rousseau and Witold Bagniewski are funded by the European Union's Horizon 2020 research and innovation program through TiPES grant no. 820970. The CHILOMOS dataset was supported by the Priority Research program of the Chinese Academy of Sciences (grants XDB03020503 and XDA05120204), and the National Basic Research program of China (973 program) (grant 2010CB950204). The LGS640 dataset was supported by by grants from the Ministry of Science and Technology of China (No. 2016YFA0601902), the Chinese Academy of Sciences (No. XDB40000000), and the National Natural Science Foundation of China (No. 41525008). The MGSQ dataset was supported by the National Basic Research program of China (2004CB720208 and 2001CCB00100), National natural Science Foundation of China (40121303 and 40331001). This is an LDEO contribution and TiPES contribution (# xxx). The authors would like to thank

Prof. Chenglong Deng for his invitation to contribute to that special issue honoring Prof. Guo Zhengtang, a long-time colleague and friend. We thank two anonymous reviewers and Prof. Jef Vandenberghe who contributed to improve the original manuscript.

Code availability

The codes used for KS and RQA analyses are part of the TiPES statistical toolbox available on GitHub at https://github.com/paleojump/TiPES_statistical_toolbox .

Bibliography

An, Z., 2000. The history and variability of the East Asian paleomonsoon climate. Quat. Sci. Rev. 19, 171–187. https://doi.org/10.1016/S0277-3791(99)00060-8

An, Z., Sun, Y., Zhou, W., Liu, W., Qiang, X., Wang, X., Xian, F., Cheng, P., Burr, G.S., 2014. Chinese loess and the East Asian monsoon, in An. Z. (Ed.): Late Cenozoic Climate Change in Asia: Loess, Monsoon and Monsoon-Arid Environment Evolution, Developments in Paleoenvironmental Research. Springer Science, Dordrecht, pp. 23–143.

An, Z.S., Kukla, G., Porter, S.C., Xiao, J.L., 1991. Magnetic susceptibility evidence of monsoon variation on the loess plateau of Central China during the last 130,000 years. Quat. Res. 36, 29–36.

Bagniewski, W., Ghil, M., Rousseau, D.D., 2021. Automatic detection of abrupt transitions in paleoclimate records. Chaos 31. https://doi.org/10.1063/5.0062543

Bagniewski, W., Rousseau, D.-D., Ghil, M., 2023. The PaleoJump database for abrupt transitions in past climates. Sci. Rep. 13. https://doi.org/10.1038/s41598-023-30592-1

Boers, N., Ghil, M., Rousseau, D.D., 2018. Ocean circulation, ice shelf, and sea ice interactions explain Dansgaard-Oeschger cycles. Proc. Nat. Acad. Sci. USA 115, E11005–E11014. https://doi.org/10.1073/pnas.1802573115

Cheng, H., Edwards, R.L., Sinha, A., Spotl, C., Yi, L., Chen, S.T., Kelly, M., Kathayat, G., Wang, X.F., Li, X.L., Kong, X.G., Wang, Y.J., Ning, Y.F., Zhang, H.W., 2016. The Asian monsoon over the past 640,000 years and ice age terminations. Nature 534, 640–646. https://doi.org/10.1038/nature18591

Clark, P.U., Archer, D., Pollard, D., Blum, J.D., Rial, J.A., Brovkin, V., Mix, A.C., Pisias, N.G., Roy, M., 2006. The middle Pleistocene transition: characteristics. mechanisms, and implications for long-term changes in atmospheric PCO2. Quat. Sci. Rev. 25, 3150–3184. https://doi.org/10.1016/j.quascirev.2006.07.008

Clark, P.U., Pollard, D., 1998. Origin of the middle Pleistocene transition by ice sheet erosion of regolith. Paleoceanography 13, 1–9.

Dansgaard, W., Johnsen, S.J., Clausen, H.B., Dahi-Jensen, D., Gundestrup, N.S., Hammer, C.U., Hvidberg, C.S., Steffensen, J.P., Sveinbjöprnsdottir, A.E., Jouzel, J., Bond, G., 1993. Evidence for general instability of past climate from a 250-kyr ice-core record. Nature 364, 218-220.

Ding, Z., Derbyshire, E., Yang, S., Yu, Z., Xiong, S., Liu, T., 2002. Stacked 2.6-Ma grain size record from the Chinese loess based on five sections and correlation with the deep-sea delta O-18 record. Paleoceanography 17. https://doi.org/10.1029/2001PA000725

Ding, Z., Liu, T., Rutter, N.W., Yu, Z., Guo, Z., ZHu, R., 1995. Ice-Volume Forcing of East Asian Winter Monsoon Variations in the Past 800,000 Years. Quat. Res. 44, 149–159.

Ding, Z., Rutter, N., Sun, J., Yang, S., Liu, T., 2000. Re-arrangement of atmospheric circulation at about 2.6 Ma over northern China: evidence from grain size records of loess-palaeosol and red clay sequences. Quat. Sci. Rev. 19, 547–558. https://doi.org/10.1016/S0277-3791(99)00017-7

Ding, Z.L., Xiong, S.F., Sun, J.M., Yang, S.L., Gux, Z.Y., Liu, T.S., 1999. Pedostratigraphy and paleomagnetism of a ~7.0 Ma

eolian loess-red clay sequence at Lingtai, Loess Plateau, north-central China and the implications for paleomonsoon evolution. Palaeogeogr., Palaeoclimatol., Palaeoecol. 152.

Eckmann, J.P., Kamphorst, S.O., Ruelle, D., 1987. Recurrence plots of dynamical systems. Europhys. Lett. 4, 973–977. https://doi.org/10.1209/0295-5075/4/9/004

Guo, Z.T., Ruddiman, W.F., Hao, Q.Z., Wu, H.B., Qiao, Y.S., Zhu, R.X., Peng, S.Z., Wei, J.J., Yuan, B.Y., Liu, T.S., 2002. Onset of Asian desertification by 22 Myr ago inferred from loess deposits in China. Nature 416, 159–163.

Hodell, D.A., Channell, J.E.T., 2016. Mode transitions in Northern Hemisphere glaciation: co-evolution of millennial and orbital variability in Quaternary climate. Clim. Past 12, 1805–1828. https://doi.org/10.5194/cp-12-1805-2016

Kindler, P., Guillevic, M., Baumgartner, M., Schwander, J., Landais, A., Leuenberger, M., 2014. Temperature reconstruction from 10 to 120 kyr b2k from the NGRIP ice core. Clim. Past 10, 887–902. https://doi.org/10.5194/cp-10-887-2014

Kukla, G., An, Z.S., 1989. Loess stratigraphy in central China. Palaeogeogr., Palaeoclimatol., Palaeoecol. 72, 203–225.

Lai, Z., Wintle, A., Thomas, D., 2007. Rates of dust deposition between 50 ka and 20 ka revealed by OSL dating at Yuanbao on the Chinese Loess Plateau. Palaeogeogr. Palaeoclimatol. Palaeoecol. 248, 431–439. https://doi.org/10.1016/j.palaeo.2006.12.013

Li, F., Rousseau, D.-D., Wu, N., Hao, Q., Pei, Y., 2008. Late Neogene evolution of the East Asian monsoon revealed by terrestrial mollusk record in Western Chinese Loess Plateau: From winter to summer dominated sub-regime. Earth Planet. Sci. Lett. 274, 439–447. https://doi.org/10.1016/j.epsl.2008.07.038

Li, F., Wu, N., Pei, Y., Hao, Q., Rousseau, D.-D., 2006. Wind-blown origin of Dongwan late Miocene-Pliocene dust sequence documented by land snail record in western Chinese Loess Plateau. Geology 34, 405–408. https://doi.org/10.1130/G22232.1

Lisiecki, L.E., Raymo, M.E., 2005. A Pliocene-Pleistocene stack of 57 globally distributed benthic delta O-18 records. Paleoceanography 20, PA1003, doi:10.1029/2004PA001071.

Liu, T., Ding, Z., 1998. Chinese loess and the paleomonsoon. Annu. Rev. Earth Planet. Sci. 26, 111–145.

Liu, T.S., and collaborators, 1985. Loess and the environment. China Ocean Press, Beijing.

Lu, H., Vandenberghe, J., An, Z., 2001. Aeolian origin and palaeoclimatic implications of the “Red Clay” (north China) as evidenced by grain-size distribution. J. Quat. Sci. 16, 89–97. https://doi.org/10.1002/1099-1417(200101)16:1<89::AID-JQS578>3.0.CO;2-8

Lu, Y.C., Wang, X.L., Wintle, A.G., 2007. A new OSL chronology for dust accumulation in the last 130,000 yr for the Chinese Loess Plateau. Quat. Res. 67, 152–160.

Marwan, N., Carmen Romano, M., Thiel, M., Kurths, J., 2007. Recurrence plots for the analysis of complex systems. Phys. Rep. 438, 237–329. https://doi.org/10.1016/j.physrep.2006.11.001

Marwan, N., Schinkel, S., Kurths, J., 2013. Recurrence plots 25 years later - Gaining confidence in dynamical transitions. EPL 101. https://doi.org/10.1209/0295-5075/101/20007

Naafs, B.D.A., Hefter, J., Stein, R., 2013. Millennial-scale ice rafting events and Hudson Strait Heinrich(-like) Events during the late Pliocene and Pleistocene: a review. Quat. Sci. Rev. 80, 1–28. https://doi.org/10.1016/j.quascirev.2013.08.014

Pisias, N.G., Moore, T.C., 1981. The evolution of Pleistocene climate: A time-series approach. Earth Planet. Sci. Lett. 52, 450–458. https://doi.org/10.1016/0012-821x(81)90197-7

Qiang, X.K., An, Z.S., Song, Y.G., Chang, H., Sun, Y.B., Liu, W.G., Ao, H., Dong, J.B., Fu, C.F., Wu, F., Lu, F.Y., Cai, Y.J., Zhou, W.J., Cao, J.J., Xu, X.W., Ai, L., 2011. New eolian red clay sequence on the western Chinese Loess Plateau linked to onset of Asian desertification about 25 Ma ago. Sci. China-Earth Sci. 54, 136–144. https://doi.org/10.1007/s11430-010-4126-5

Rasmussen, S.O., Bigler, M., Blockley, S.P., Blunier, T., Buchardt, S.L., Clausen, H.B., Cvijanovic, I., Dahl-Jensen, D.,

Johnsen, S.J., Fischer, H., Gkinis, V., Guillevic, M., Hoek, W.Z., Lowe, J.J., Pedro, J.B., Popp, T., Seierstad, I.K., Steffensen, J.P., Svensson, A.M., Vallelonga, P., Vinther, B.M., Walker, M.J.C., Wheatley, J.J., Winstrup, M., 2014. A stratigraphic framework for abrupt climatic changes during the Last Glacial period based on three synchronized Greenland ice-core records: refining and extending the INTIMATE event stratigraphy. Quat. Sci. Rev. 106, 14–28. https://doi.org/10.1016/j.quascirev.2014.09.007

Rousseau, D., Bagniewski, W., Ghil, M., 2022. Abrupt climate changes and the astronomical theory: are they related? Clim. Past 18, 249–271. https://doi.org/10.5194/cp-18-249-2022

Rousseau, D.D., Boers, N., Sima, A., Svensson, A., Bigler, M., Lagroix, F., Taylor, S., Antoine, P., 2017a. (MIS3 & 2) millennial oscillations in Greenland dust and Eurasian aeolian records - A paleosol perspective. Quat. Sci. Rev. 169, 99–113. https://doi.org/10.1016/j.quascirev.2017.05.020

Rousseau, D.D., Svensson, A., Bigler, M., Sima, A., Steffensen, J.P., Boers, N., 2017b. Eurasian contribution to the last glacial dust cycle: how are loess sequences built? Clim. Past 13. https://doi.org/10.5194/cp-13-1181-2017

Ruddiman, W.F., Raymo, M., Martinson, D.G., Clement, B.M., Backman, J., 1989. Pleistocene evolution : Northern Hemisphere ice sheets and North Atlantic Ocean. Paleoceanography, 4, 353–412.

Sima, A., Kageyama, M., Rousseau, D.D., Ramstein, G., Balkanski, Y., Antoine, P., Hatté, C., 2013. Modeling dust emission response to North Atlantic millennial-scale climate variations from the perspective of East European MIS3 loess deposits. Clim. Past 9, 1385–1402. https://doi.org/10.5194/cpd-9-143-2013

Sima, A., Rousseau, D.-D., Kageyama, M., Ramstein, G., Schulz, M., Balkanski, Y., Antoine, P., Dulac, F., Hatté, C., 2009. Imprint of North-Atlantic abrupt climate changes on western European loess deposits as viewed in a dust emission model. Quat. Sci. Rev. 28, 2851–2866. https://doi.org/10.1016/j.quascirev.2009.07.016

Sun, D., Su, R., Bloemendal, J., Lu, H., 2008. Grain-size and accumulation rate records from Late Cenozoic aeolian sequences in northern China: Implications for variations in the East Asian winter monsoon and westerly atmospheric circulation. Palaeogeogr. Palaeoclimatol. Palaeoecol. 264, 39–53. https://doi.org/10.1016/j.palaeo.2008.03.011

Sun, Y., An, Z., Clemens, S., Bloemendal, J., Vandenberghe, J., 2010. Seven million years of wind and precipitation variability on the Chinese Loess Plateau. Earth Planet. Sci. Lett. 297, 525–535. https://doi.org/10.1016/j.epsl.2010.07.004

Sun, Y., Clemens, S., An, Z., Yu, Z., 2006. Astronomical timescale and palaeoclimatic implication of stacked 3.6-Myr monsoon records from the Chinese Loess Plateau. Quat. Sci. Rev. 25, 33–48. https://doi.org/10.1016/j.quascirev.2005.07.005

Sun, Y., Clemens, S., Guo, F., Liu, X., Wang, Y., Yan, Y., Liang, L., 2021. High-sedimentation-rate loess records: A new window into understanding orbital- and millennial-scale monsoon variability. Earth-Sci. Rev. 220. https://doi.org/10.1016/j.earscirev.2021.103731

Sun, Y., Clemens, S.C., Morrill, C., Lin, X., Wang, X., An, Z., 2012. Influence of Atlantic meridional overturning circulation on the East Asian winter monsoon. Nature Geosci. 5, 46–49.

Sun, Y., Yan, Y., Nie, J., Li, G., Shi, Z., Qiang, X., Chang, H., An, Z., 2020. Source-to-sink fluctuations of Asian aeolian deposits since the late Oligocene. Earth-Sci. Rev. 200. https://doi.org/10.1016/j.earscirev.2019.102963

Wang, Y., Cheng, H., Edwards, R.L., Kong, X., Shao, X., Chen, S., Wu, J., Jiang, X., Wang, X., An, Z., 2008. Millenial- and orbital-scale changes in the East Asian monsoon over the past 224,000 years. Science 451, 1090–1093.

Wang, Y.J., Cheng, H., Edwards, R.L., An, Z.S., Wu, J.Y., Shen, C.C., Dorale, J.A., 2001. A high-resolution absolute-dated Late Pleistocene monsoon record from Hulu Cave, China. Science 294, 2345–2348. https://doi.org/10.1126/science.1064618

Wolff, E.W., Chappellaz, J., Blunier, T., Rasmussen, S.O., Svensson, A., 2010. Millennial-scale variability during the last glacial: The ice core record. Quat. Sci. Rev. 29, 2828–2838. https://doi.org/10.1016/j.quascirev.2009.10.013

Xiao, J., Porter, S.C., An, Z., Kumai, H., Yoshikawa, S., 1995. Grain size of quartz as an indicator of winter monsoon strength on the Loess Plateau of Central China during the last 130,000 Yr. Quat. Res. 43, 22–29.

Xu, Y., Yue, L., Li, J., Sun, L., Sun, B., Zhang, J., Ma, J., Wang, J., 2009. An 11-Ma-old red clay sequence on the Eastern Chinese Loess Plateau. Palaeogeogr., Palaeoclimatol., Palaeoecol. 284, 383–391. https://doi.org/10.1016/j.palaeo.2009.10.023

Yang, S., Ding, Z., 2014. A 249 kyr stack of eight loess grain size records from northern China documenting millennial-scale climate variability. Geochem. Geophys. Geosyst. 15, 798–814. https://doi.org/10.1002/2013gc005113

Zbilut, J., Webber, C., 1992. Embeddings and delays as derived from quantification of recurrence plots. Phys. Lett. A 171, 199–203. https://doi.org/10.1016/0375-9601(92)90426-M

Figure captions

Fig. 1. KS test applied on two high-resolution records, the Greenland NGRIP (Rasmussen et al., 2014) and the Hulu cave (Wang et al., 2001, 2008) $\delta^{18}O$ records over the past 122 kyrs. The records are compared in three panels of 46 kyrs each, labeled a, b, and c from youngest to oldest. The grey bars represent interstadials according to Bagniewski et al. (2021), with Greenland interstadials labeled GIx and Chinese interstadials labeled Ax. The red and blue bars indicate, abrupt warmings/coolings detected in NGRIP and abrupt moisture increase/drying in the speleothem records, respectively. The red and blue triangles depict the common abrupt warming/moisture and cooling/drying transitions. The NGRIP time scale is in ka b2K while the Hulu time scale is in kyr BP.

Fig. 2. KS test applied to the Chinese composite speleothem $\delta^{18}O$ (Cheng et al., 2016) and the CHILOMOS grain-size (Yang and Ding, 2014) records over the past 250 kyrs. Same caption as in **Fig.** 1 but the Chinese interstadials during the penultimate climate cycle (250 ka -130 ka) are labeled Bx. Likewise, Chinese stadials are labeled SAx or SBx. In CHILOMOS diagrams, the blue bars correspond to abrupt increase in grain size, while red bars correspond to abrupt fining of the transported quartz particles. The events labeled in italics on the CHILOMOS panels correspond to events identified in Yang and Ding (2014) but not identified by the KS test. The timescale of both records is in kyr BP.

Fig. 3. Recurrence Quantification Analysis (RQA) of CS. Top: the $\delta^{18}O$ record, middle: recurrence plot (RP) corresponding to a symmetric matrix with time on the vertical and horizontal axes, bottom: recurrence rate (RR) analysis with minima marked with pink crosses, using their respective prominence shown in **Table** 1.

Fig. 4. RQA of CHILOMOS. Same caption as in **Fig.** 3. RR results are given in **Table** 2.

Fig. 5 KS test of the LGS640 grain size record (Sun et al., 2021) split into three panels of 220 kyrs each. Same caption as in **Fig.** 2.

Fig. 6 RQA of LGS640. Same caption as in **Fig.** 3.

Fig. 7. KS test of the Mean Grain-Size of Quartz particles (MGSQ) (Sun et al., 2006) in three panels of 1,200 kyrs each. Top panel is the youngest and bottom panel is the oldest. Blue bars represent the odd marine isotope stages while the red ones correspond to terminations. MIS x on top of each panel represents the abrupt transition towards marine isotope stage (MIS) "x" according to Lisiecki and Raymo (, 2005). The grey bars identify interglacials or groups of interglacials. The green triangle as indicated in **Fig.** 8 (see **Table** 6).

Fig. 8. RQA of MGSQ. Same convention as in **Fig.** 3. The green triangles identify the transitions with the highest prominence values, as indicated in **Fig.** 6 (see **Table** 6).

Table 1 KS test of the NGRIP and Hulu cave $\delta^{18}O$ for the last climate cycle. Comparison of the dates of abrupt warmings/moistening (left) and cooling/drying transitions (right). Labels for NGRIP according to Rasmussen et al. (2014) and for Hulu cave according to Wang et al. (2008).

Table 2 KS test of the Chinese speleothem $\delta^{18}O$ and of the CHILOMOS grain-size composite for the last two climate cycles. Comparison of the dates of abrupt moistening (left) and drying transitions (right). Labels for the moistening

transitions in the Chinese speleothem are from Wang et al. (2008) and in CHILOMOS from Yang and Ding (2014). The labels of the drying in CHILOMOS are from the present study

Table 3 RQA of the Chinese speleothem $\delta^{18}O$ and of the CHILOMOS grain-size composite for the last two climate cycles. Dates of the minima are identified by the RR prominence, shown together with the equivalent transitions detected by the KS method. For easier reading, the dates have been re-ordered from younger to older. The most significant minima are highlighted in yellow. The original ranking is given in Suppl. Tab 1.

Table 4 KS test of the Chinese speleothem $\delta^{18}O$ and of the LGS640 dataset for the last 640 Myrs. Comparison of the dates of abrupt moistening and drying transitions in both records. The dates found in both records are highlighted in red and in blue for drying or moistening events respectively.

Table 5 RQA of the LGS640 grain-size composite for the last seven climate cycles. Dates of the minima are identified by the RR prominence. The most significant minima (RR prominence >0.5) are highlighted in yellow.

Table 6 KS test and RQA of MGSQ grain dataset for the last 3.6 Myrs. In this analysis the moistening and drying transitions is labeled as warming and cooling. On the left, KS results with the corresponding marine isotope stage (MIS) boundaries. On the right, RQA results with minima ordered according their prominence value. Dates with RR>0.6 are highlighted in yellow.

Appendices:

Table A.1. Abrupt transitions over the past 130 kyrs BP from the NGRIP, Chinese Speleothem and CHILOMOS records. Identification of the common abrupt warmings or moistenings on the left, and abrupt coolings or dryings on the right. Differences between the highest and lowest transition dates. Indication of the NGRIP and Chinese interstadials and stadials (GI-GS and A-SA respectively).

Table A.2. RQA of the 250 kyrs Chinese speleothem and CHILOMOS records ranked according the RR prominence, the chronology. Indication of the time difference between the identified transitions.

Table A.3. Comparison of the KS-test results from the LGS 640 and the Chinese speleothem over the past 650 kyrs. Indication of the Marine isotope stratigraphy and the number of cool and warm transitions and the percentage of drying events per climate cycle

Fig.1

a

b

NGRIP

Chinese speleothem

Age (ka b2K)

$\delta^{18}O$ [‰]

GI-1e GI-2.2 GI-3 GI-4 GI-5.2 GI-6 GI-7 GI-8c GI-9 GI-10 GI-11 GI-12c

A1 A2 A3 A4 A5 A6 A7 A8 A9 A10 A11 A12

GI-12c GI-13 GI-14e GI-15.1 GI-15.2 GI-16.2 GI-17.2 GI-18 GI-19.1 GI-19.2 GI-20.c GI-21.1e

A12 A13 A14 A15 A16 A17 A18 A19 A20 A21

Fig.1 ctd

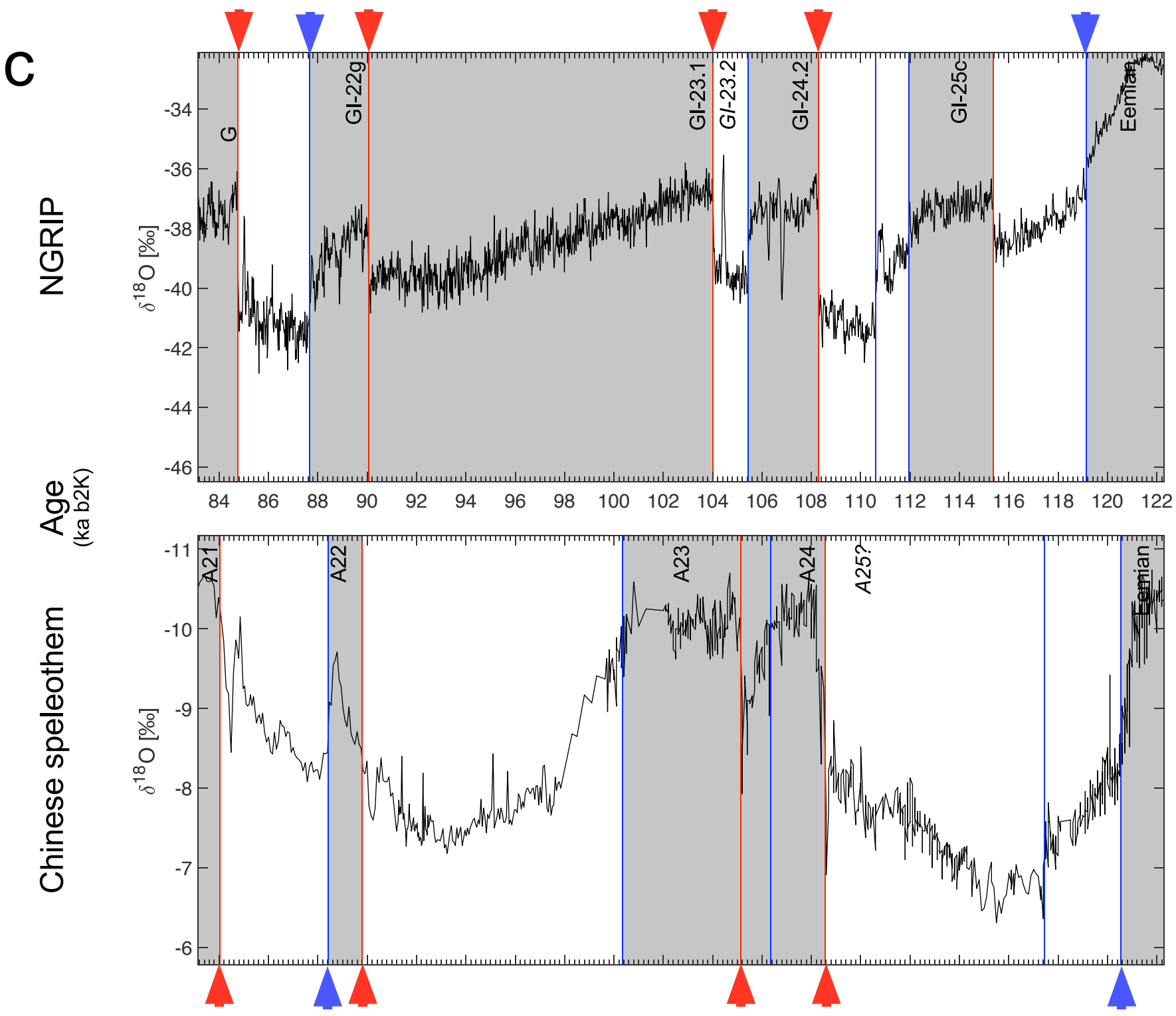
C
NGRIP
Age (ka b2K)
δ^{18}O [‰]
-34
-36
-38
-40
-42
-44
-46
84
86
88
90
92
94
96
98
100
102
104
106
108
110
112
114
116
118
120
122
G
GI-22g
GI-23.1
GI-23.2
GI-24.2
GI-25c
Eemian
Chinese speleothem
δ^{18}O [‰]
-11
-10
-9
-8
-7
-6
A21
A22
A23
A24
A25?
Eemian

Fig. 2

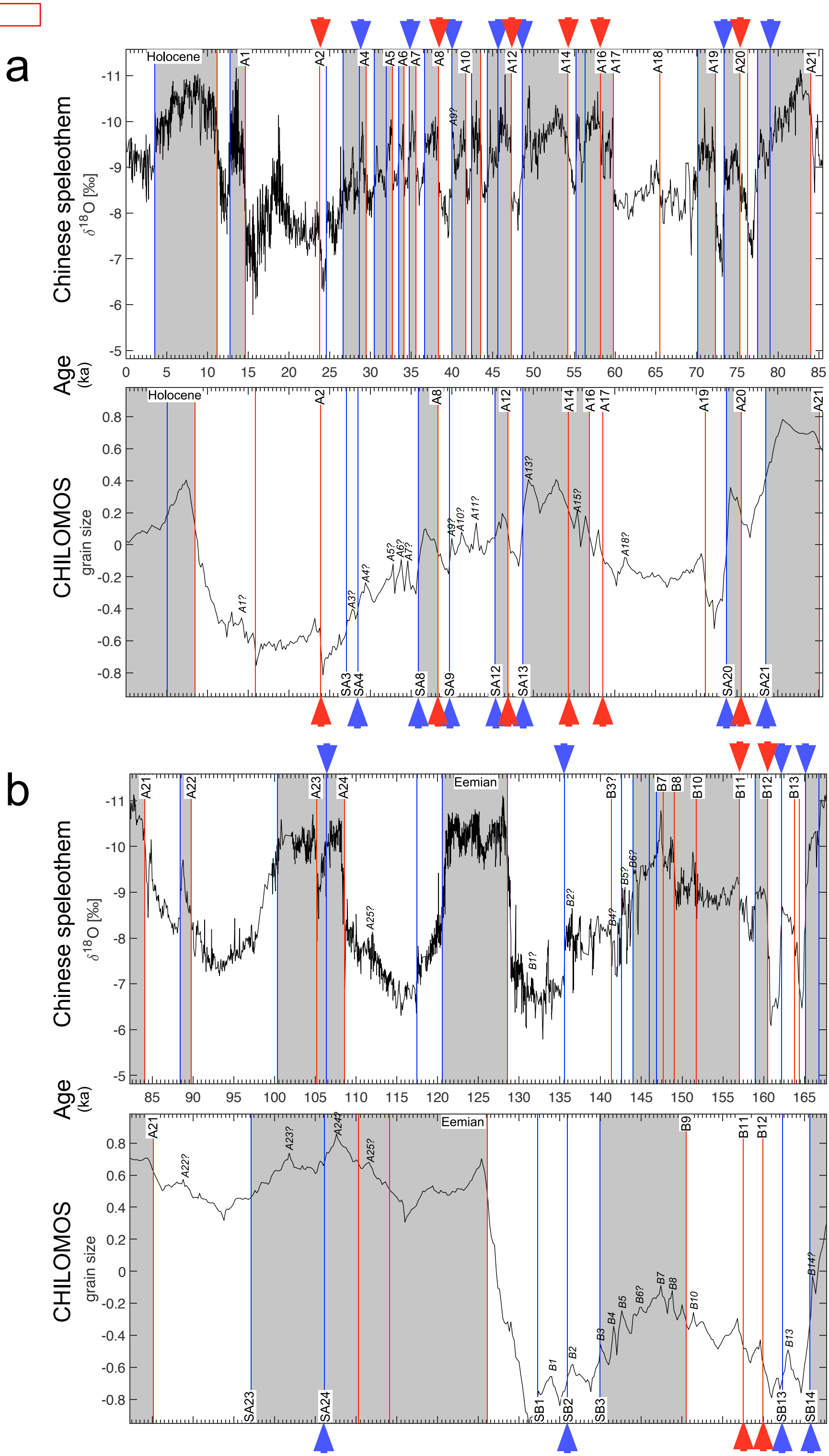
a
Chinese speleothem
δ^{18}O [‰]
Holocene
A1
A2
A4
A5
A6
A7
A8
A10
A12
A14
A16
A17
A18
A19
A20
A21
A19?
Age (ka)
CHILOMOS
grain size
A1?
A3?
A4?
A5?
A6?
A7?
A9?
A10?
A11?
A13?
A15?
A18?
SA3
SA4
SA8
SA9
SA12
SA13
SA20
SA21
b
Eemian
A22
A23
A24
B3?
B7
B8
B10
B11
B12
B13
A22?
A23?
A24?
A25?
B1?
B2?
B4?
B5?
B6?
B1
B2
B3
B4
B5
B6?
B7
B8
B10
B9
B13
B14?
SA23
SA24
SB1
SB2
SB3
SB13
SB14

Fig. 2 ctd

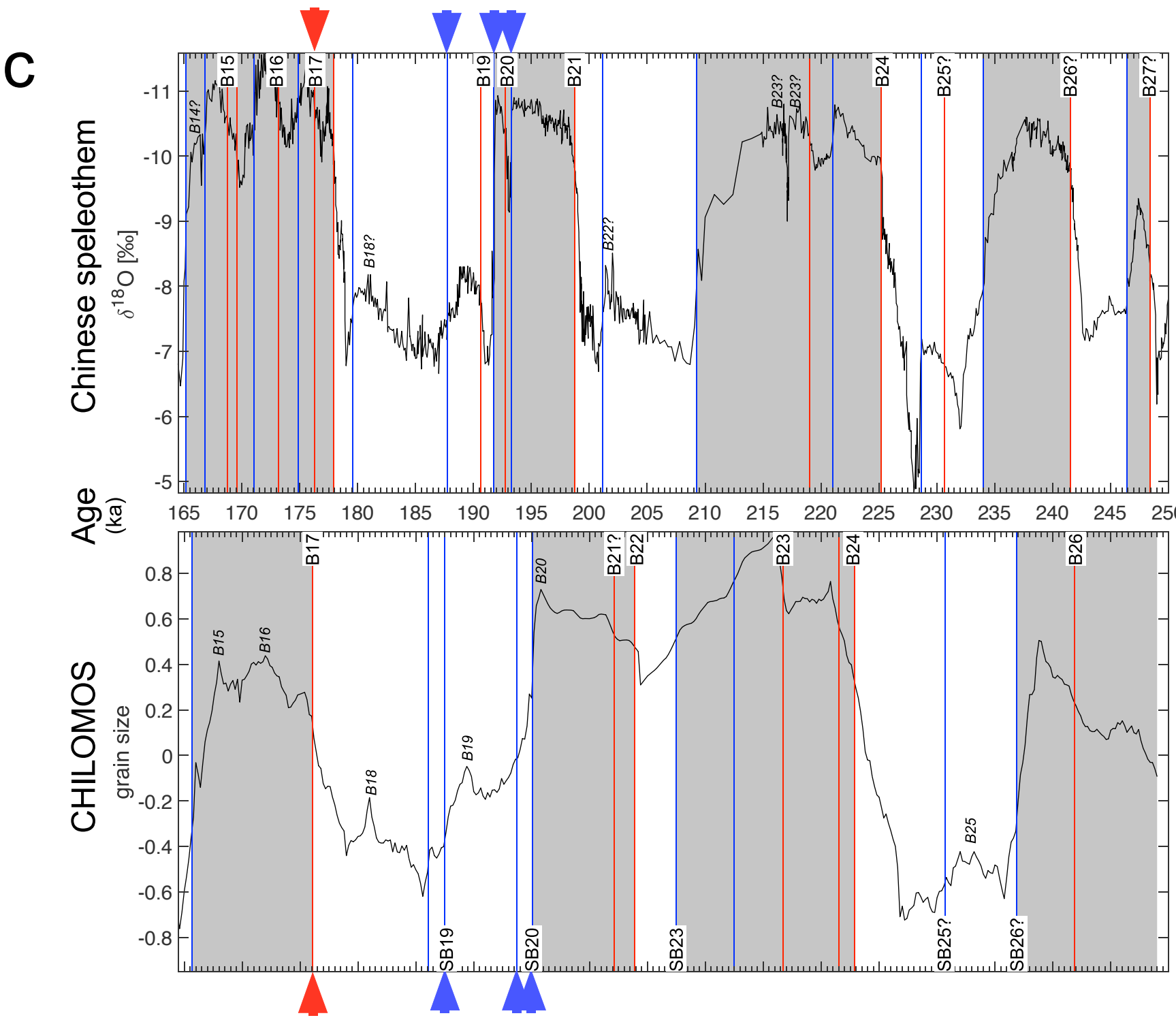
C
Chinese speleothem
$\delta^{18}O$ [‰]
-11
-10
-9
-8
-7
-6
-5
B14?
B15
B16
B17
B18?
B19
B20
B21
B22?
B23?
B23?
B24
B25?
B26?
B27?
Age (ka)
165
170
175
180
185
190
195
200
205
210
215
220
225
230
235
240
245
250
CHILOMOS
grain size
0.8
0.6
0.4
0.2
0
-0.2
-0.4
-0.6
-0.8
B15
B16
B17
B18
B19
B20
B21?
B22
B23
B24
B25
B26
SB19
SB20
SB23
SB25?
SB26?

Fig. 3

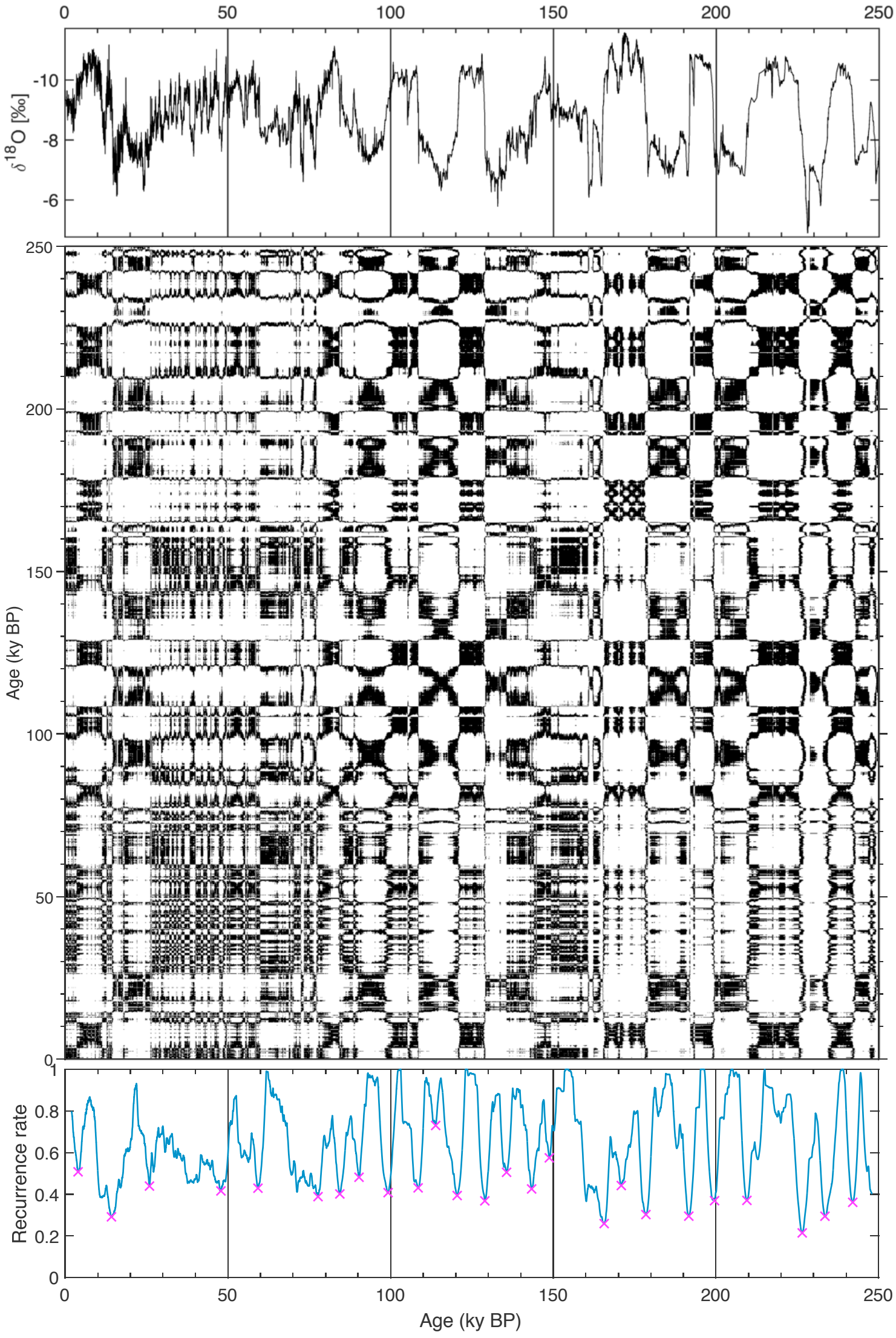
0
50
100
150
200
250
$\delta^{18}O$ [‰]
-10
-8
-6
Age (ky BP)
Recurrence rate
0
0.2
0.4
0.6
0.8
1

Fig. 4

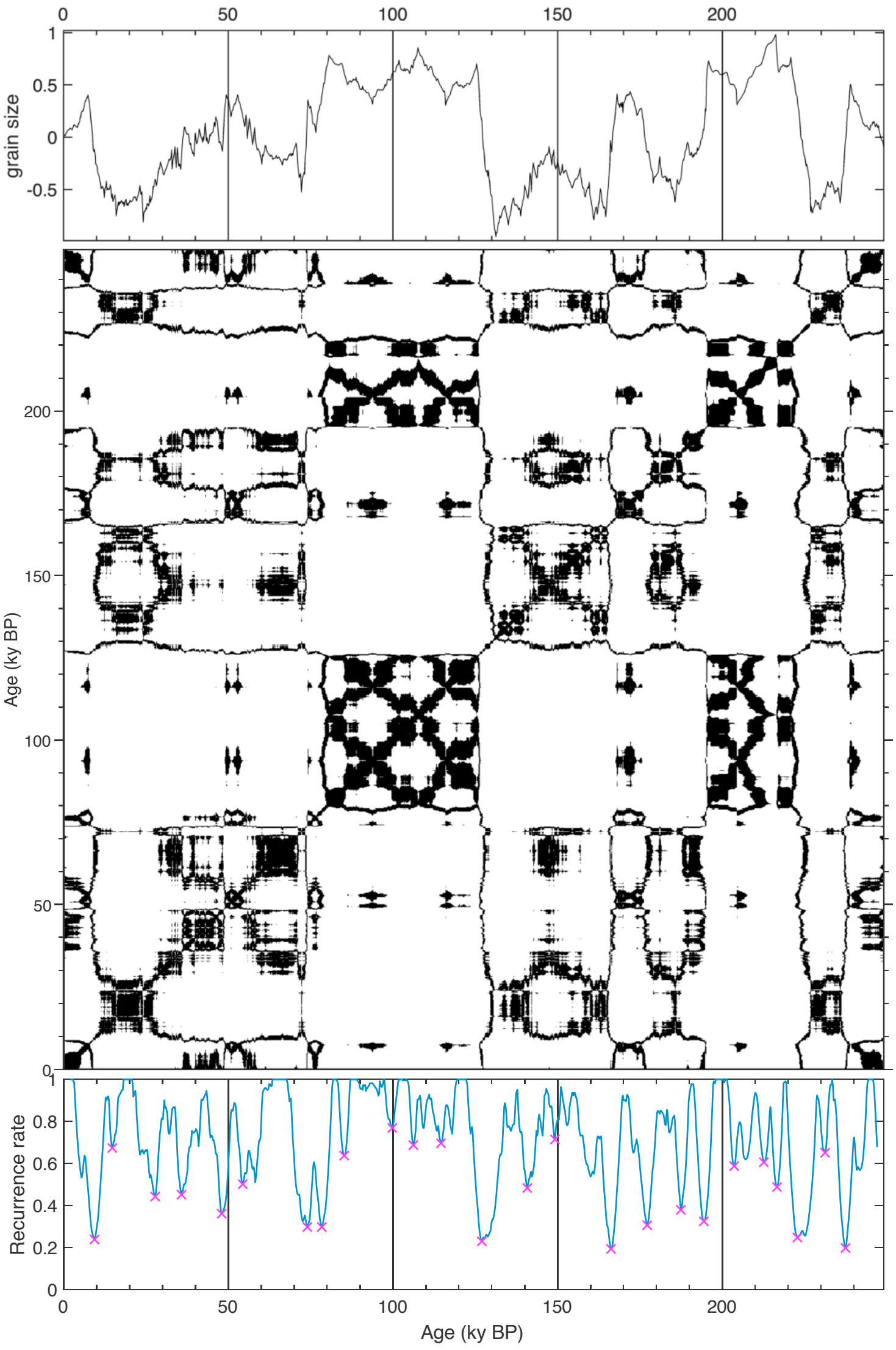

Fig. 5

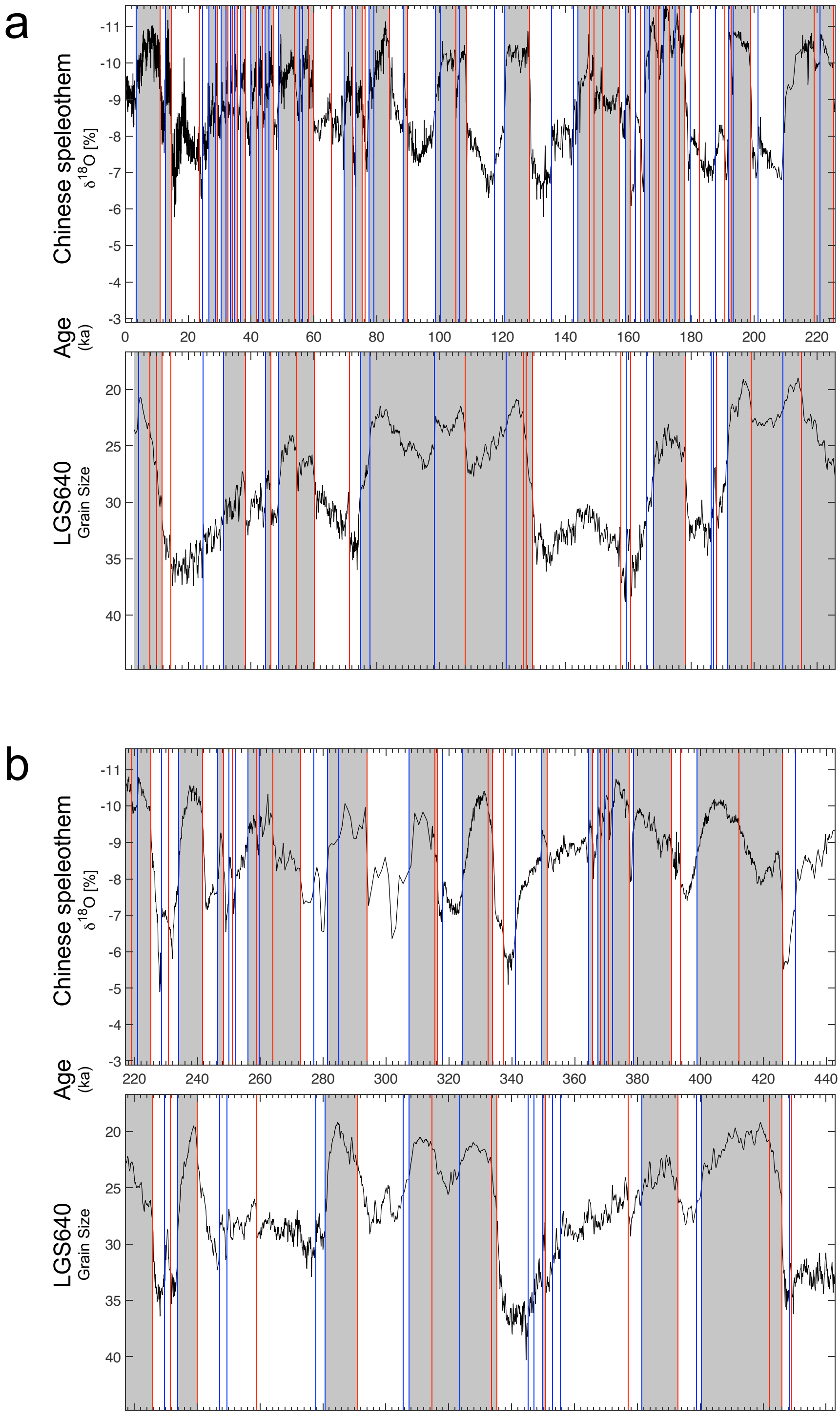
a
Chinese speleothem
δ18O [%]
-11
-10
-9
-8
-7
-6
-5
-4
-3
0
20
40
60
80
100
120
140
160
180
200
220
Age
(ka)
LGS640
Grain Size
20
25
30
35
40
b
Chinese speleothem
δ18O [%]
-11
-10
-9
-8
-7
-6
-5
-4
-3
220
240
260
280
300
320
340
360
380
400
420
440
Age
(ka)
LGS640
Grain Size
20
25
30
35
40

Fig. 5 ctd

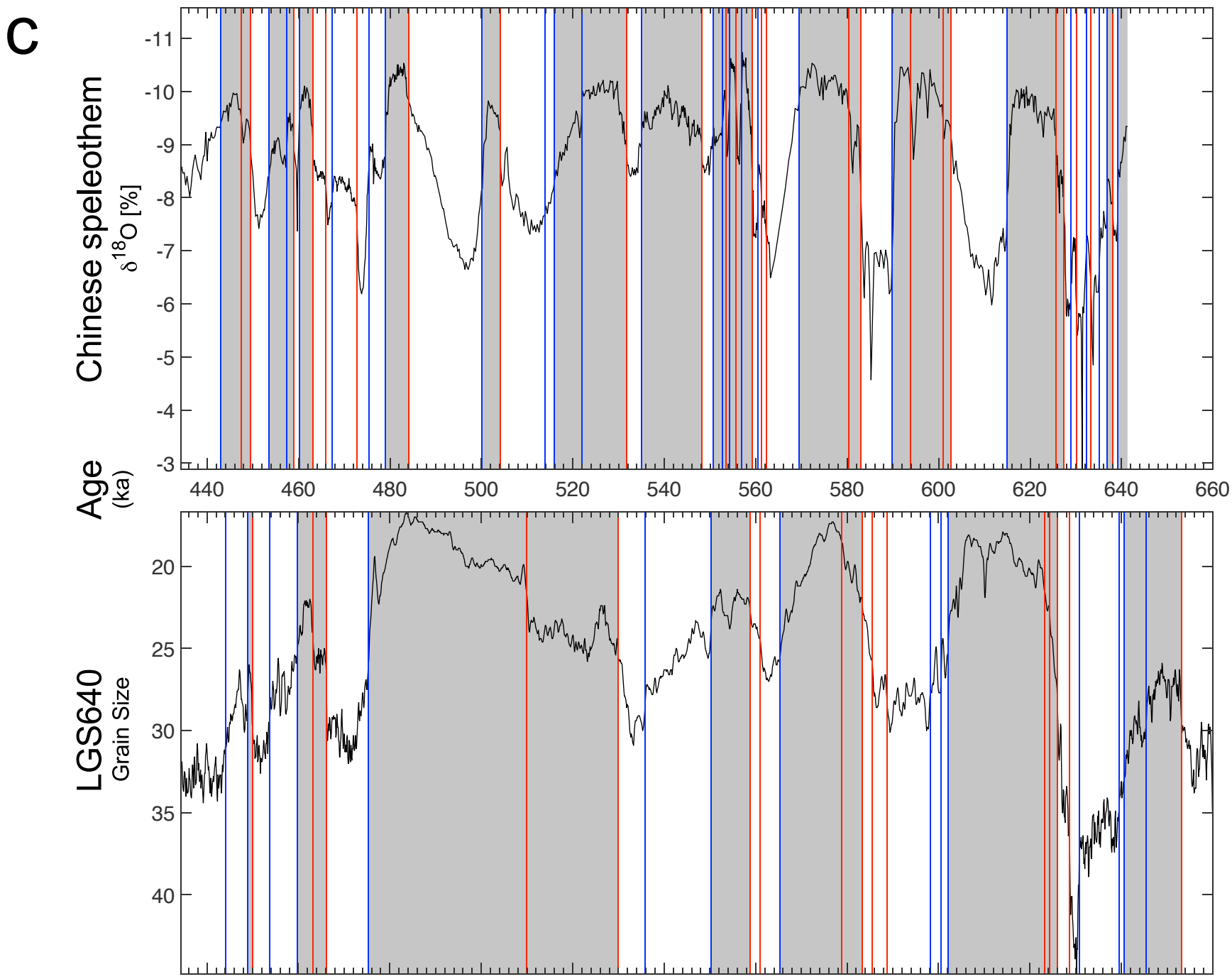
C
Chinese speleothem
δ18O [‰]
-11
-10
-9
-8
-7
-6
-5
-4
-3
Age
(ka)
440
460
480
500
520
540
560
580
600
620
640
660
LGS640
Grain Size
20
25
30
35
40

Fig. 6

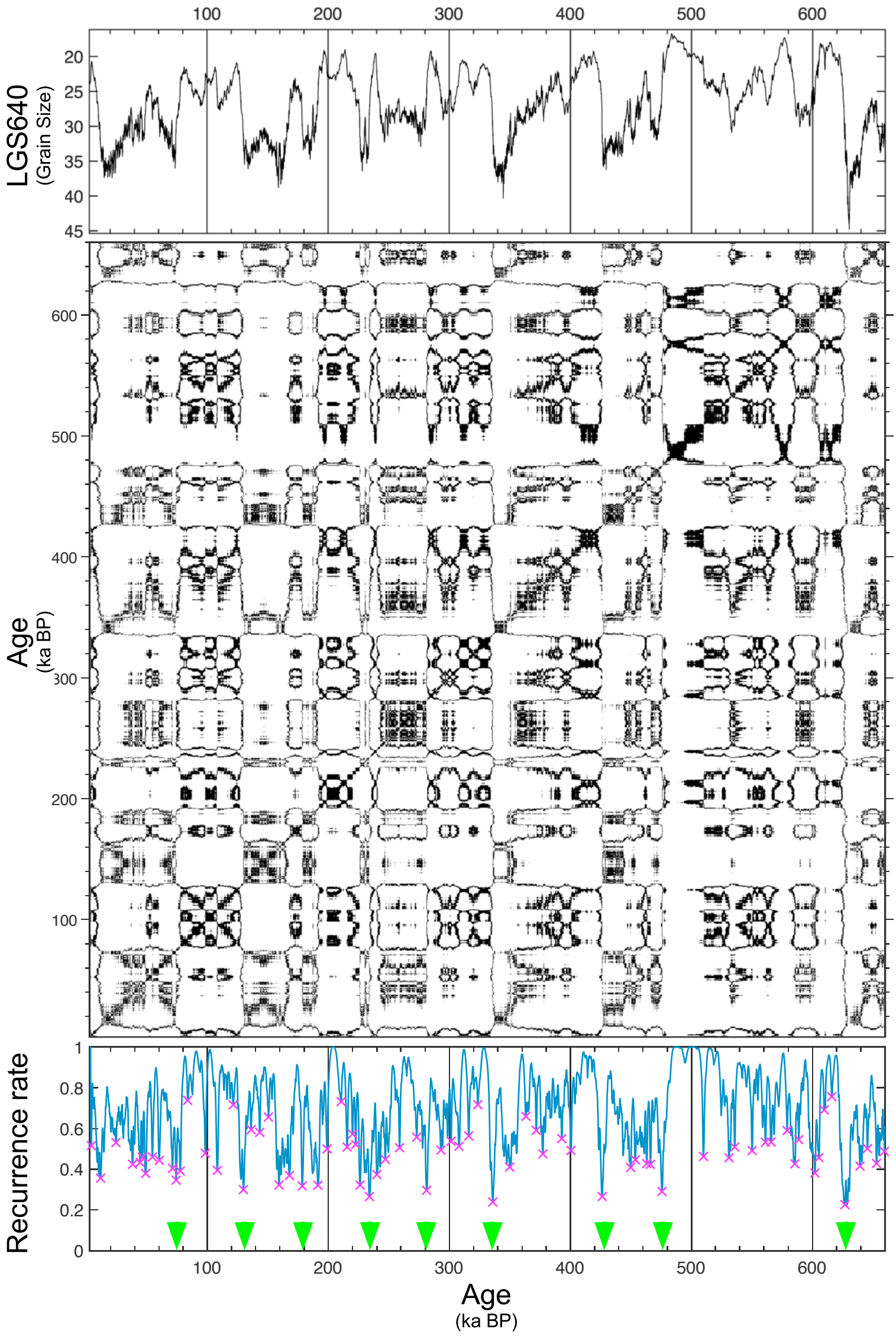
LGS640
(Grain Size)
100
200
300
400
500
600
20
25
30
35
40
45
Age
(ka BP)
600
500
400
300
200
100
Recurrence rate
1
0.8
0.6
0.4
0.2
0
100
200
300
400
500
600
Age
(ka BP)

Fig. 7

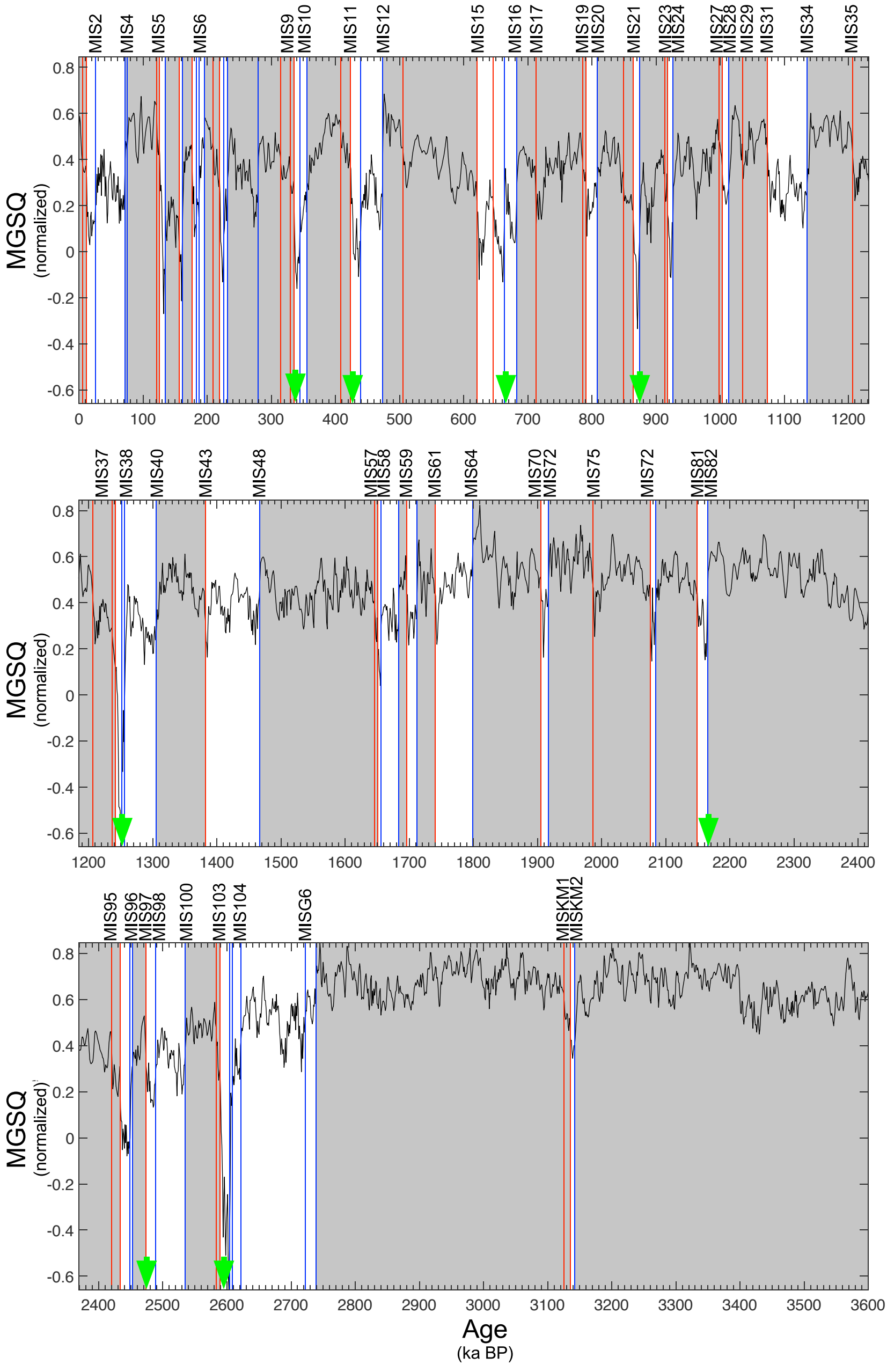
MIS2
MIS4
MIS5
MIS6
MIS9
MIS10
MIS11
MIS12
MIS15
MIS16
MIS17
MIS19
MIS20
MIS21
MIS23
MIS24
MIS27
MIS28
MIS29
MIS31
MIS34
MIS35
MIS3
MIS3
MIS4
MIS4
MIS4
MIS5
MIS5
MIS5
MIS6
MIS6
MIS7
MIS7
MIS7
MIS7
MIS8
MIS8
MIS95
MIS96
MIS97
MIS98
MIS100
MIS103
MIS104
MISG6
MISKM1
MISKM2
MGSQ
(normalized)
Age
(ka BP)

Fig. 8

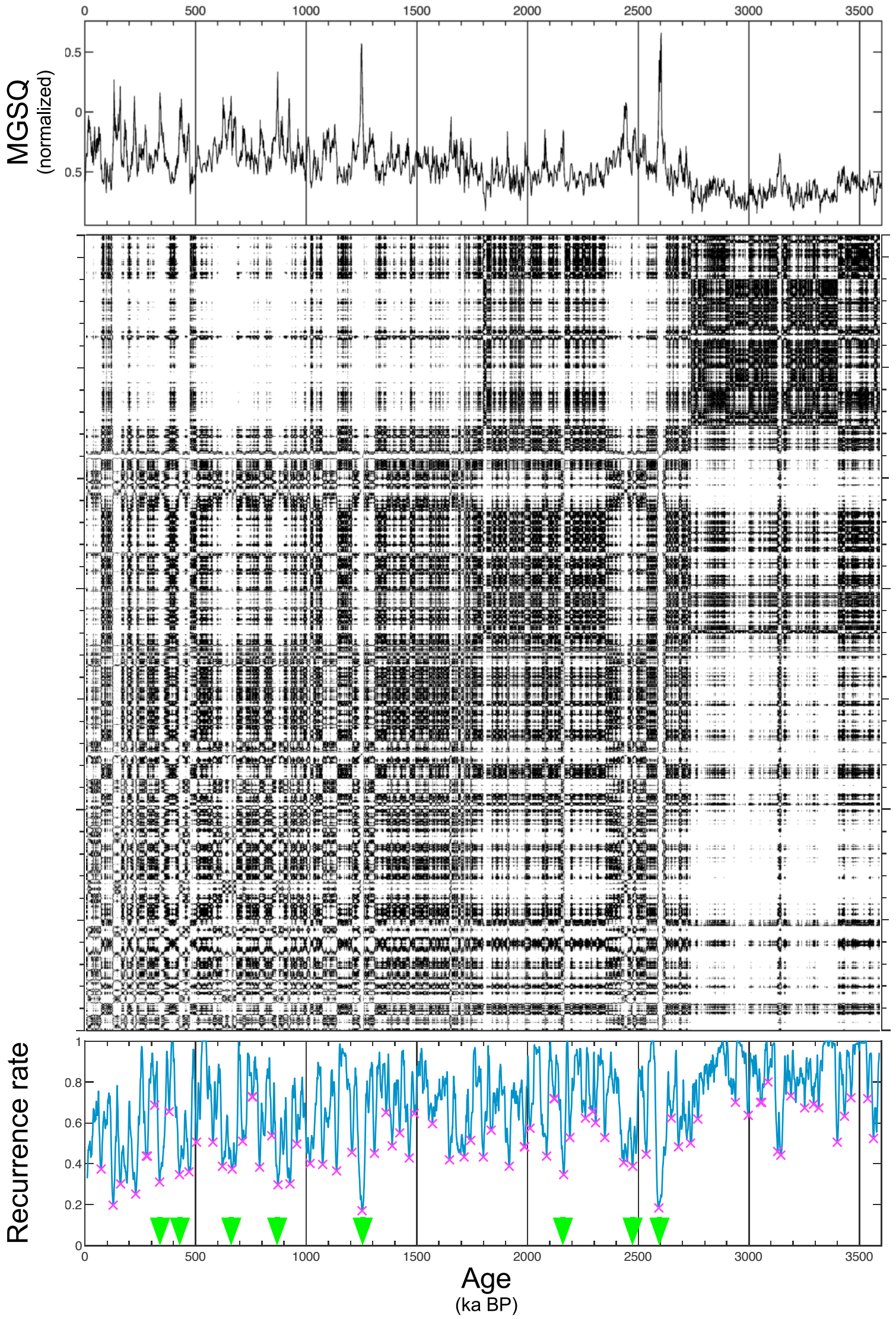
MGSQ
(normalized)
0
500
1000
1500
2000
2500
3000
3500
0.5
0
0.5
Recurrence rate
1
0.8
0.6
0.4
0.2
0
Age
(ka BP)

Table 1

NGRIP δ18O KS window: 0.6 - 4 ky warming in ka BP		NGRIP GI	Hulu cave δ18O KS window: 0.6 - 4 ky warming/moistening ka BP	NGRIP GI	Chinese #	NGRIP δ18O KS window: 0.6 - 4 ky cooling in ka BP		NGRIP GS	Hulu cave δ18O KS window: 0.6 - 4 ky cooling/drying in ka BP	NGRIP GS
11,68	1	11.4 event	11,19						3,50	?
14,68	1	GI-1e	14,62		A1	13,26	1	GI-1b	12,78	
			23,76	GI-2.2?	A2				24,59	GS-3 3d dust peak
			29,43	GI-4?	A4				26,65	GS-3 1st dust peak
32,54	1	GI-5.2	32,68		A5				28,63	GS-4
			34,07	GI-6?	A6				30,42	GS-5.1
35,58	1	GI-7c	35,54		A7	31,98	1	GS-5.2	31,90	
38,22	1	GI-8c	38,31		A8	33,36	1	GS-06	33,42	
41,54	1	GI-10	41,68		A10	34,74	1	GS-07	34,75	
43,36	1	GI-11	43,49		A11	37,06	1	GI_08b	36,61	
46,84	1	GI-12c	47,25		A12				39,96	GS-9
54,22	1	GI-14e	54,21		A14	40,92		GS10		
58,04	1	GI-16.2	58,21		A16	42,34	1	GS-11	42,39	
59,50	1	GI-17.2	59,79		A17				44,31	GS-12
			65,48	?	A18	45,18		?	45,61	?
72,34	1	GI-19.2	72,29		A19	48,46	1	GS-13	48,64	
76,44	1	GI-20c	75,33		A20	51,66		GI-14b		
			76,25	?		56,58		GS-15.2	55,23	GS-15.2
84,76	1	GI-21.1e	84,03		A21				56,32	GS-16.1
90,06	1	GI-22g	89,79		A22	70,38	1	GS-19.2	70,16	
104,02	1	GI-23.1	105,15		A23	74,18	1	GS-20	73,35	
108,30	1	GI-24.2	108,55		A24	77,84	1	GS-21.1	77,51	
115,38		GI-25c							78,99	GI-21.1b
						80,74		?		
						87,66	1	GS-22	88,43	
									100,35	?
						105,44		GS-24.1		
									106,35	GI-24.1b
						110,60		GS-25		
						111,94		GI-25b?		
									117,45	?
						119,14	1	GS-26	120,55	

Table 2

China speleothem δ18O KS window: 0.6 - 4 ky moistening in Ka BP	Chinese #	CHILOMOS grain size KS window: 0.6 - 4 ky moistening in Ka BP	Chinese #	China speleothem δ18O KS window: 0.6 - 4 ky drying in ka BP	CHILOMOS grain size KS window: 0.6 - 4 ky drying in ka BP	Chinese # (this study)
		8,500		3,500		
11,187					5,100	
14,617	A1			12,779		
		15,900	*?*	24,590		
23,755	A2	23,900	*A2*	26,650		
29,430	A4				27,100	SA3
32,675	A5			28,625	28,500	SA4
34,065	A6			30,420		
35,535	A7			31,900		
38,305	A8	38,300	*A8*	33,420		
41,675	A10			34,750	35,900	SA8
43,490	A11			36,605		
47,250	A12	46,900	*A12*	39,955	39,700	SA9
54,205	A14	54,300	*A14*	42,390		
		56,900	*A16*	44,305		
58,210	A16	58,500	*A17*	45,605	45,300	SA12
59,785	A17			48,635	48,700	SA13
65,480	A18			55,230		
72,285	A19	71,100	*A19*	56,320		
75,330	A20	75,500	*A20*	70,155		
76,245				73,350	73,700	SA20
84,030	A21	85,100	*A21*	77,510		
89,790	A22			78,990	78,500	SA21
105,150	A23			88,425		
108,550	A24				97,100	SA23
		110,300		100,350		
		114,100		106,350	106,100	SA24
				117,450		
128,550	Eemian	126,100	*Eemian*	120,550		
141,300	B3?				132,300	SB1
147,650	B7			135,550	135,900	SB2
149,050	B8				139,900	SB3
		150,500	*B9*	142,550		
151,750	B10			143,950		
157,050	B11	157,500	*B11*	145,950		
160,500	B12	159,900	*B12*	146,850		
163,800	B13			158,950		
164,400				162,200	162,300	SB13
168,750	B15			165,150	165,700	SB14
169,550				166,800		
173,150	B16			171,050		
176,250	B17	176,100	*B17*	174,850		
177,950	?			179,550		
190,650	B19				186,100	
192,750	B20			187,750	187,500	SB19
198,750	B21			191,750		
		202,100	*B21*		193,700	
		203,900	*B22*	193,250	195,100	SB20
219,050	B23?	216,700	*B23*	201,150		
225,200	B24	221,500	*B24*		207,500	SB23
		222,900	*?*	209,250		
230,650	*B25*				212,500	
241,550	*B26*	241,900	*B26?*	221,050		
248,450	*B27*			228,650		
					230,700	SB25?
				234,000		
					236,900	SB26?
				246,450		
				250,050		

Table 3

China cave δ18O RQA window: 4 ky, epsilon: 0.6 ka BP	RR prominence	KS detection		CHILOMOS grain size RQA window: 4 ky, epsilon: 0.12 ka BP	RR prominence	KS detection
1,96	0,2884					
				7,40	0,7619	
12,22	0,5748	KS-SA1		12,80	0,2449	ND-KS/SA1
23,9	0,2877	KS-A2		25,80	0,5034	ND-KS/SA3
				33,80	0,4490	
45,86	0,5151	KS-SA12		46,00	0,6395	KS-A12
57,24	0,4439			52,40	0,3855	
				72,00	0,7029	
75,7	0,6014	KS-A20		76,40	0,7029	KS-SA21
82,4	0,3756	ND-KS/A21		83,20	0,3628	ND-KS/A21
88,3	0,2940					
97,24	0,5738	ND-KS/A23.1		97,80	0,2313	KS-SA23
106,46	0,5288			104,20	0,3129	
111,86	0,2269	ND-KS	trans GI15 in NGRIP this study	112,60	0,2313	ND-KS
118,46	0,6057					
				125,00	0,7347	
126,96	0,6312					
133,64	0,3764					
				138,80	0,4671	
141,34	0,4829					
146,78	0,2781	KS-SB7		147,20	0,2404	ND-KS/B7
163,64	0,7403	KS-SB13		164,20	0,8073	ND-KS/B13
168,9	0,2341					
				175,20	0,6213	
176,46	0,4980					
				185,40	0,4762	
189,64	0,6840					
				192,40	0,6531	
197,56	0,6304					
				201,60	0,3492	
207,5	0,6282					
				210,60	0,2630	
				214,60	0,5034	
				220,80	0,7528	
224,5	0,7850					
				229,20	0,2721	
231,48	0,4943					
				235,40	0,8027	
240,02	0,6218					

Table 4

Chinese speleothem δ18O	LGS640 grain size	Com. event	Diff. Com.	Chinese speleothem δ18O	LGS640 grain size	Com. event	Diff. Com.
KS window 0.6-4 ky moistening in ka BP	KS window: 0.5-4 ky moistening in ka BP		in ka BP	KS window 0.6-4 ky drying in ka BP	KS window: 0.5-4 ky drying in ka BP		in ka BP
				3,500			
	7,850				4,150		
	10,050			12,779			
11,187	11,650	1	-0,464	24,590	24,650	1	-0,060
14,617	14,450	1	0,167	26,650			
23,755				28,625			
29,430				30,420			
32,675				31,900	31,250	1	0,650
34,065				33,420			
35,535				34,750			
38,305	38,150	1	0,155	36,605	36,850	1	-0,245
41,675				39,955			
43,490				42,390			
	46,350			44,305	44,650	1	-0,345
47,250				45,605			
54,205	54,450	1	-0,245	48,635	48,650	1	-0,015
58,210					49,450		
59,785				55,230			
	60,050			56,320			
65,480				70,155			
	71,250			73,350	74,250	1	-0,900
72,285				77,510	77,250	1	0,260
75,330				78,990			
76,245				88,425			
84,030					97,350		
89,790				100,350			
105,150				106,350			
108,550	107,950	1	0,600	117,450			
	126,650			120,550			
	127,450				121,150		
128,550				135,550			
	129,650			142,550			
141,300				143,950			
147,650				145,950			
149,050				146,850			
151,750				158,950			
157,050	157,550	1	-0,500	162,200	159,250	1	2,950
160,500	160,750	1	-0,250	165,150	165,650	1	-0,500
163,800				166,800			
164,400					168,050		
168,750				171,050			
169,550				174,850			
173,150				179,550			
176,250					186,350		
177,950	178,050	1	-0,100	187,750	187,050	1	0,700
	187,950						
190,650				191,750	191,650	1	0,100
192,750				193,250			
198,750	198,950	1	-0,200	201,150			
	214,950			209,250	209,150		
219,050				221,050			
225,200	225,950	1	-0,750	228,650			
230,650	230,850	1	-0,200		229,850		
	231,450			234,000	233,850	1	0,150
				246,450	247,150	1	-0,700
	240,150			250,050	249,750	1	0,300
241,550				252,250			
248,450				256,050			
251,150				259,750			
258,750	258,850	1	-0,100	276,950	277,750	1	-0,800
264,000				281,400	280,750	1	0,650
272,850					305,550		
	291,150				307,650		
293,900				318,050			
315,450	314,650	1	0,800	324,150	323,450	1	0,700
316,250				341,150			
333,650	333,550	1	0,100		345,250		
	335,350				347,150		
337,350				349,550	349,750	1	-0,200
351,150	350,950	1	0,200				

Table 4 ctd

365,550					352,950		
368,100					355,550		
370,750				364,350			
377,350	377,150	1	0,200	367,150			
391,100				369,550			
393,600	392,850	1	0,750	371,700			
412,250				372,650			
	422,150			378,650			
425,800	425,950	1	-0,150		381,350		
				398,850	398,850	1	0,000
	429,150				400,250		
447,400				429,000	428,450		
449,450	449,950	1	-0,500	430,150			
	455,850			442,950			
458,900					444,050		
463,250	463,250	1	0,000		448,850		
465,950	466,150	1	-0,200	453,650	453,650	1	0,000
472,650				457,600			
483,550				460,150	459,750		
504,150				467,350			
	509,950			475,200	475,250	1	-0,050
	529,950			479,050			
531,750				500,100			
548,250				518,250			
553,550				521,950			
555,800				535,000	535,850	1	-0,850
559,150	558,850	1	0,300		550,350		
561,250	560,950	1	0,300	551,950			
562,250				552,700			
	578,850			554,200			
580,800				556,950			
582,950	583,250			560,450			
	584,950				565,350		
	588,750			567,550			
593,500				589,800			
600,950					598,150		
602,700					600,550		
	623,050				602,150		
	624,350			614,900			
625,650	625,950	1	-0,300	628,850			
627,400				632,300	630,750	1	1,550
	628,650			635,400			
629,950				636,800			
633,300				639,200	639,550	1	-0,350
638,100					640,650		
					645,550		
					653,150		
					656,350		

Table 5

LGS640
grain size
RQA window: 1 - 8 ky, epsilon = 1.2

ka BP	RR prominence
626,9	0,773585158
335,9	0,760512766
233,9	0,730522263
426,3	0,709052921
129,8	0,699873418
281,2	0,65616999
74,2	0,641385854
178,4	0,595589197
475,7	0,591446855
159,2	0,579054775
602,1	0,578984379
11,8	0,542514245
510	0,531236545
108,3	0,515938954
531,1	0,513376717
585,5	0,509428361
98,3	0,500729869
377,3	0,489413621
191,4	0,489067898
550,2	0,431810611
653	0,431060492
49	0,424159402
316	0,423243814
258,8	0,403233553
400,5	0,395220553
349,8	0,388427285
561,2	0,382796142
54,6	0,370317226
215,5	0,362029728
38,2	0,358437254
293	0,35296604
240,1	0,351407322
60,3	0,348444615
449,8	0,341725934
307,9	0,33109935
198,9	0,329038565
226,2	0,324491933
466,2	0,323019536
565,8	0,321000689
4,1	0,30566718
463,1	0,305246929
639,4	0,298513521
392,9	0,294710319
535,8	0,281938395
143,3	0,279747842
371,8	0,268966237
363,3	0,261274824
301,4	0,256837007
222,6	0,254255806
44,4	0,249674758
453,7	0,239480907
247,1	0,23438373
24,5	0,224067961

Table 5 ctd

ka BP	RR prominence
645,5	0,218944992
83,7	0,216671124
150,5	0,212616
77,6	0,210737226
659,5	0,206641736
616	0,202310554
71,2	0,198809554
167,8	0,198665238
609,8	0,197419629
210,6	0,190932247
136,2	0,188723762
323,5	0,186688714
605,4	0,185748714
579,2	0,181393888
121,4	0,180931278
220	0,179575953
588,8	0,178951513
46,4	0,17875264
273	0,177795747

Table 6

Chinese Loess Plateau grain size KS window: 2 - 20 ky						Chinese Loess Plateau grain size RQA window: 20 ky	
cooling	Age (ka)	MIS	warming	Age (ka)	MIS	ka BP	RR prominence
25,5	29	MIS2	5,5			1252	0,829931973
71,5	71	MIS4	11,5			2593	0,816326531
75,5			121,5			872	0,689342404
134,5			125,5	130	MIS5	337	0,662131519
161,5			156,5			427	0,648526077
183,5			176,5			2163	0,648526077
187,5	191	MIS6	209,5			665	0,621315193
195,5			219,5			2475	0,612244898
225,5			314,5	300	MIS8	1917	0,589569161
231,5			329,5			127	0,557823129
279,5			335,5	337	MIS9	3144	0,557823129
344,5			408,5			1647	0,544217687
355,5	374	MIS10	423,5			2086	0,544217687
439,5			505,5	524	MIS13	789	0,535147392
473,5	472	MIS12	620,5	621	MIS15	1800	0,535147392
663,5			645,5			229	0,530612245
682,5	676	MIS16	712,5	712	MIS17	1137	0,530612245
808,5	820	MIS20	785,5			1465	0,526077098
874,5			790,5	790	MIS19	277	0,503401361
926,5	936	MIS24	849,5			282	0,503401361
1013,5	1014	MIS28	864,5	866	MIS21	3399	0,494331066
1135,5	1141	MIS34	913,5			2682	0,471655329
1251,5			917,5	917	MIS23	1074	0,462585034
1255,5	1264	MIS38	998,5	982	MIS27	1388	0,458049887
1305,5	1304	MIS40	1003,5			504	0,453514739
1466,5	1469	MIS48	1034,5	1031	MIS29	1308	0,444444444
1655,5	1670	MIS58	1073,5	1081	MIS31	2191	0,439909297
1683,5			1206,5	1190	MIS35	712	0,430839002
1711,5			1236,5			2536	0,430839002
1798,5	1800	MIS64	1241,5	1244	MIS37	926	0,421768707
1916,5	1915	MIS72	1382,5			1017	0,421768707
2084,5			1645,5	1642.5	MIS57	2349	0,41723356
2165,5	2168	MIS82	1650,5			3563	0,41723356
2448,5			1695,5	1697.5	MIS59	1206	0,412698413
2452,5	2452	MIS96	1740,5	1743	MIS61	161	0,403628118
2488,5	2494	MIS98	1905,5	1898	MIS71	1713	0,394557823
2534,5	2540	MIS100	1986,5	1990	MIS75	578	0,380952381
2604,5			2075,5	2088	MIS78	73	0,371882086
2608,5			2148,5	2146	MIS81	2307	0,362811791
2621,5	2614	MIS104	2420,5	2425	MIS95	2997	0,358276644
2722,5	2630	G6	2433,5			2011	0,353741497
2738,5			2473,5	2477	MIS97	2261	0,340136054
3142,5	3150	KM2	2583,5			1985	0,326530612
			2589,5	2595	MIS103	1987	0,326530612
			3125,5	3119	KM1	957	0,321995465
			3135,5			1835	0,321995465

Suppl. Table 1

NGRIP δ18O KS window: 0.6 - 4 ky warming in ka BP	NGRIP GI	China speleothem δ18O KS window: 0.6 - 4 ky moistening in ka BP	China speleothem δ18O KS window: 0.6 - 4 ky moistening in ka BP	Chinese #	CHILOMOS grain size KS window: 0.6 - 4 ky moistening in ka BP	Com (3)	Diff. Com. in ka BP	NGRIP δ18O KS window: 0.6 - 4 ky cooling in ka BP	NGRIP GS	China speleothem δ18O KS window: 0.6 - 4 ky drying in ka BP	China speleothem δ18O KS window: 0.6 - 4 ky drying in ka BP	CHILOMOS grain size KS window: 0.6 - 4 ky drying in ka BP	Chinese # (this study)	Com (3)	Diff. Com. in ka BP
					8,500				?	3,500	3,500				
11,680	11.4 event	11,187	11,187									5,100			
14,680	GI-1e	14,617	14,617	A1				13,260	GI-1b	12,779	12,779				
					15,900				GS-3 3d dust peak	24,590	24,590				
		23,755	23,755	A2	23,900				GS-3 1st dust peak	26,650	26,650				
		29,430	29,430	A4								27,100	SA3		
32,540	GI-5.2	32,675	32,675	A5					GS-4	28,625	28,625	28,500	SA4		
		34,065	34,065	A6					GS-5.1	30,420	30,420				
35,580	GI-7c	35,535	35,535	A7				31,980	GS-5.2	31,900	31,900				
38,220	GI-8c	38,305	38,305	A8	38,300	1	0,085	33,360	GS-06	33,420	33,420				
41,540	GI-10	41,675	41,675	A10				34,740	GS-07	34,750	34,750	35,900	SA8	1	1,160
43,360	GI-11	43,490	43,490	A11				37,060	GI_08b	36,605	36,605				
46,840	GI-12c	47,250	47,250	A12	46,900	1	0,410		GS-9	39,955	39,955	39,700	SA9		
54,220	GI-14e	54,205	54,205	A14	54,300	1	0,095	40,920	GS10						
					56,900			42,340	GS-11	42,390	42,390				
58,040	GI-16.2	58,210	58,210	A16	58,500	1	0,460		GS-12	44,305	44,305				
59,500	GI-17.2	59,785	59,785	A17				45,180	?	45,605	45,605	45,300	SA12		
		65,480	65,480	A18				48,460	GS-13	48,635	48,635	48,700	SA13	1	0,240
72,340	GI-19.2	72,285	72,285	A19	71,100			51,660	GI-14b						
76,440	GI-20c	75,330	75,330	A20	75,500	1	1,110	56,580	GS-15.2	55,230	55,230				
		76,245	76,245						GS-16.1	56,320	56,320				
84,760	GI-21.1e	84,030	84,030	A21	85,100	1	1,070	70,380	GS-19.2	70,155	70,155				
90,060	GI-22g	89,790	89,790	A22				74,180	GS-20	73,350	73,350	73,700	SA20	1	0,830
104,020	GI-23.1	105,150	105,150	A23				77,840	GS-21.1	77,510	77,510				
108,300	GI-24.2	108,550	108,550	A24					GI-21.1b	78,990	78,990	78,500	SA21		
					110,300			80,740	?						
					114,100			87,660	GS-22	88,425	88,425				
												97,100	SA23		
			128,550	Eemian	126,100				?	100,350	100,350				
								105,440	GS-24.1						
									GI-24.1b	106,350	106,350	106,100	SA24		
								110,600	GS-25						
								111,940	GI-25b?						
									?	117,450	117,450				
						6		119,140	GS-26	120,550	120,550			**3**	

Suppl. Table 2

Chinese speleothem δ18O					CHILOMOS grain size				
RQA window: 4 ky, epsilon: 0.6			ranked		RQA window: 4 ky, epsilon: 0.12			ranked	
ka BP	RR prominence	Diff. Transitions	ka BP	RR prominence	ka BP	RR prominence	Diff. Transitions	ka BP	RR prominence
224,500	0,785030074		1,960	0,288420006	164,200	0,807256236		7,400	0,761904762
163,640	0,74032821	10,260	12,220	0,574787753	235,400	0,802721088	5,400	12,800	0,244897959
189,640	0,68399297	11,680	23,900	0,287683658	7,400	0,761904762	13,000	25,800	0,503401361
126,960	0,631221999	21,960	45,860	0,51508626	220,800	0,752834467	8,000	33,800	0,448979592
197,560	0,630380436	11,380	57,240	0,443949407	125,000	0,734693878	12,200	46,000	0,639455782
207,500	0,628202272	18,460	75,700	0,601420757	72,000	0,702947846	6,400	52,400	0,385487528
240,020	0,621766788	6,700	82,400	0,375584763	76,400	0,702947846	19,600	72,000	0,702947846
118,460	0,605678077	5,900	88,300	0,29395312	192,400	0,653061224	4,400	76,400	0,702947846
75,700	0,601420757	8,940	97,240	0,573797678	46,000	0,639455782	6,800	83,200	0,362811791
12,220	0,574787753	9,220	106,460	0,528798792	175,200	0,621315193	14,600	97,800	0,231292517
97,240	0,573797678	5,400	111,860	0,226875572	25,800	0,503401361	6,400	104,200	0,31292517
106,460	0,528798792	6,600	118,460	0,605678077	214,600	0,503401361	8,400	112,600	0,231292517
45,860	0,51508626	8,500	126,960	0,631221999	185,400	0,476190476	12,400	125,000	0,734693878
176,460	0,497957971	6,680	133,640	0,376426326	138,800	0,467120181	13,800	138,800	0,467120181
231,480	0,494294696	7,700	141,340	0,482908839	33,800	0,448979592	8,400	147,200	0,240362812
141,340	0,482908839	5,440	146,780	0,278111928	52,400	0,385487528	17,000	164,200	0,807256236
57,240	0,443949407	16,860	163,640	0,74032821	83,200	0,362811791	11,000	175,200	0,621315193
133,640	0,376426326	5,260	168,900	0,234103116	201,600	0,349206349	10,200	185,400	0,476190476
82,400	0,375584763	7,560	176,460	0,497957971	104,200	0,31292517	7,000	192,400	0,653061224
88,300	0,29395312	13,180	189,640	0,68399297	229,200	0,272108844	9,200	201,600	0,349206349
1,960	0,288420006	7,920	197,560	0,630380436	210,600	0,263038549	9,000	210,600	0,263038549
23,900	0,287683658	9,940	207,500	0,628202272	12,800	0,244897959	4,000	214,600	0,503401361
146,780	0,278111928	17,000	224,500	0,785030074	147,200	0,240362812	6,200	220,800	0,752834467
168,900	0,234103116	6,980	231,480	0,494294696	97,800	0,231292517	8,400	229,200	0,272108844
111,860	0,226875572	8,540	240,020	0,621766788	112,600	0,231292517	6,200	235,400	0,802721088

Suppl. Table 3

Marine isotope stratigraphy		LGS640				CS		
Climate cycle	ky	dry	moist	% dry/ Total	Σ abrupts LGS640	dry	% dry/ Total	Σ abrupts CS
MIS2-5	14-130	14	6	70,00	20	23	51,11	45
MIS6-7	130-243	10	9	52,63	19	20	50,00	40
MIS8-9	243-337	8	4	66,67	12	9	50,00	18
MIS10-11	337-424	8	4	66,67	12	8	50,00	16
MIS12_13	424-524	12	2	85,71	14	12	57,14	21
MIS14-15	524-621	5	10	33,33	15	9	42,86	21
MIS16	621-712	7			7	5	50,00	10
					99			**171**